Published in final edited form as:
IEEE Trans Biomed Eng. 2014 May ; 61(5): 1364–1379. doi:10.1109/TBME.2014.2313619.

Magnetic Resonance Imaging at Ultrahigh Fields

Kamil Uğurbil, B.A., Ph.D.
Center for Magnetic Resonance Research (CMRR), University of Minnesota, Minneapolis, MN 55455 USA

Kamil Uğurbil: kamil@cmrr.umn.edu

Abstract

Since the introduction of 4 T human systems in three academic laboratories circa 1990, rapid progress in imaging and spectroscopy studies in humans at 4 T and animal model systems at 9.4 T have led to the introduction of 7 T and higher magnetic fields for human investigation at about the turn of the century. Work conducted on these platforms has demonstrated the existence of significant advantages in SNR and biological information content at these ultrahigh fields, as well as the presence of numerous challenges. Primary difference from lower fields is the deviation from the near field regime; at the frequencies corresponding to hydrogen resonance conditions at ultrahigh fields, the RF is characterized by attenuated traveling waves in the human body, which leads to image nonuniformities for a given sample-coil configuration because of interferences. These nonuniformities were considered detrimental to the progress of imaging at high field strengths. However, they are advantageous for parallel imaging for signal reception and parallel transmission, two critical technologies that account, to a large extend, for the success of ultrahigh fields. With these technologies, and improvements in instrumentation and imaging methods, ultra-high fields have provided unprecedented gains in imaging of brain function and anatomy, and started to make inroads into investigation of the human torso and extremities. As extensive as they are, these gains still constitute a prelude to what is to come given the increasingly larger effort committed to ultrahigh field research and development of ever better instrumentation and techniques.

Index Terms

Functional imaging (fMRI); high field; magnetic resonance imaging (MRI); neuroimaging

I. Introduction

The explosion of magnetic resonance imaging (MRI) and spectroscopy (MRS) research at ultrahigh magnetic fields (7 T and above) is such that it is already a difficult task to comprehensively cover it in a brief review or not to accidentally overlook some of it; I apologize for such omissions in advance. The focus in this review is largely on biological applications that have provided the initial impetus for the development of ultrahigh field MR and solutions to its technological challenges; as such, this paper contains a significant focus

on work done in the center I lead [the Center for Magnetic Resonance Research (CMRR)] and on applications, such as functional brain imaging in particular and neuroimaging in general, which has been a central research theme of our group. Interested readers are also referred to several other recent reviews on 7 T work where clinical applications receive more attention (e.g., [1]–[9]).

II. Historical Overview

The desire to extract biological information from intact biological systems nondestructively using MRI and MRS and the development of functional magnetic resonance imaging (fMRI) introduced new disruptive technologies that allowed the study of the human brain activity with unprecedented detail and resolution. These developments also catalyzed the pursuit of numerous new techniques and instrumentation, including the development of ultrahigh magnetic fields for imaging the human brain and ultimately the rest of the human body.

In 1980s, at a time when high-end clinical MRI scanners operated at 1.5 T, efforts to examine 4 T for human imaging were undertaken by the three major manufacturers of clinical MRI instruments. Initial results from these companies, obtained in their research laboratories, produced inferior and undesirable 4 T brain images [see Fig. 1(a)] and highlighted more problems than advantages at this high field [10], [11]. It was clear that going to 4 T would require significant new investment in research and development; it was not going to be as simple as changing the frequency of the electronics and the RF coils. Likely because of these conclusions, the industry abandoned the high field effort at the time and these 4 T systems ended up in three academic laboratories one of which was the CMRR at the University of Minnesota.

The 4 T system designated for CMRR was made available for us before it was shipped to Minneapolis. Mike Garwood from CMRR used this opportunity to demonstrate for the first time the feasibility of obtaining superior T_1 weighted anatomical images of the human brain at 4 T [see Fig. 1(b)]. These images, obtained with a sequence named MDEFT, were reported much later in a review paper [12] and in a journal article [13] but were first presented at a conference in Whistler in 1990. The success of the MDEFT approach at 4 T came from the relative B_1 insensitivity of the sequence [12], thus avoiding the problems arising from nonuniform B_1s that increasingly plague imaging at magnetic fields higher than $\sim$1.5 T. Immediately after the 4 T system was installed in Minneapolis and became operational, one of the two studies that simultaneously and independently introduced functional brain imaging [14], [15] was carried out on this system [14].

We became interested in functional imaging at magnetic fields higher than 4 T because of the successes at 4 T as well as early work on modeling of the functional imaging signals showing a strong dependence on magnetic field magnitude (e.g., [16]– [19]; also see [20] and references therein). After initial studies conducted on animal models at 9.4 T, we initiated discussions with Magnex in 1995 that resulted in the successful development of a 7 T, 90 cm bore magnet for the first time. We established a 7 T human system in CMRR in 1999 using this magnet and components obtained from various manufacturers. The system was assembled in house by us.

This first ever “lego” 7 T human MR system was less than ideal but the work coming from this system (e.g., [21]–[33]) started the trend for rapidly increasing number of 7 T systems. An 8 T/80-cm bore human system was installed at Ohio State shortly before our 7 T was delivered. Beautiful gradient recalled echo images of brain anatomy were produced from this system (e.g., [34] and references therein). Ultimately, however, it was the 7 T work that defined the path of ultrahigh fields.

Human fMRI, one of the main reasons we pushed to ultra-high fields, reached new levels of spatial resolution and specificity at 7 T (discussed further on). Spectroscopy measurements with ^{1}H and X- nuclei (e.g., ^{31} P, ^{17}O, and ^{23}Na) obtained at 7 T have provided neurochemical and metabolic information in the human brain with increasing biomedical relevance (e.g., [26], [35]–[42]). Unique kinetic studies of *intracellular* enzymatic rates that were previously possible only in cells in suspension or perfused organs, such as the magnetization transfer measurement of ATP turnover rates (e.g., [43], [44]), originally introduced in 1977 [45], was performed two decades later for the first time in the human brain at 7 T [41]. More improvements are expected as a consequence of the recent focus on higher order shimming techniques (e.g., [46], [47]).

Until recently, all the ultrahigh field studies were conducted in the brain. But feasibility of imaging in the human torso at 7 T, a more challenging goal due to the relative dimensions of the object *versus* the RF wavelength, was demonstrated in 2008 and 2009 [48]–[51], thus starting a new burgeoning activity in several laboratories.

Because of this large body of work, 7 T is rapidly becoming the most advanced platform for biomedical research in humans, delivering ever more informative results as increasing number of laboratories acquire 7 T instruments of amassed sophistication produced commercially from major manufacturers of MRI scanners. New peaks are expected at ultrahigh field human MR applications as existing 9.4 T scanners are increasingly employed for human studies and the 10.5 and 11.7 T systems that are planned for installation in 2014 and 2015 come online.

In the following sections, 7 T work briefly mentioned above and some of the other ultrahigh field accomplishments and challenges will be reviewed.

III. Field Dependence of SNR

In all MR applications, SNR is critical for image quality, measurement time, and/or spatial resolution. However, SNR becomes rather complex when high magnetic fields (hence high radio frequencies) are considered with conductive biological samples. The primary reason for this is that with increasing magnetic fields, the wavelength of the RF that must be employed for spin excitation and signal detection becomes increasingly shorter in conductive tissues of the human body, and smaller then dimensions of the object to be imaged. In other words, the *relative object size* becomes greater than 1; this is the case in the human head and particularly in the human torso at 7 T. Consequently, one operates no longer in the near field regime; instead the RF behavior is characterized as an attenuated traveling wave [32].

Fig. 2 illustrates calculations from [32] showing gray scale 2-D plots of instantaneous transverse $|B_1|$ at progressing time points, generated by a surface coil placed on one side of a spherical phantom; the calculations are presented for three different conductivities of the sample. At zero conductivity, a one-wavelength standing wave (i.e., a "resonance") is established (leftmost column, Fig. 2); under this condition, excitation is simply not possible in certain areas, such as the middle of this standing wave. At higher conductivities approximating human tissue (rightmost column, Fig. 2), the RF wave is attenuated and a more familiar surface coil profile emerges. These calculations were experimentally verified at 7 T [32]. Because of this behavior, image signal intensity can become highly nonuniform. To quote directly from the abstract in [32], "The characteristic image intensity distribution in the human head is the result of spatial phase distribution and amplitude modulation by the interference of the RF traveling waves determined by a given sample-coil configuration."

Because of the "attenuated traveling wave" nature of the RF, the SNR can be expected to be nonuniform at high fields in the human body. This was demonstrated when transmit B_1 (B_1^+) field profile and SNR was examined in the human head for 4 and 7 T carefully, using the same coil structure (a TEM "volume" head coil), taking into account measured instrumental and coil performance differences [21]. Even though the volume coil employed in this particular study produced a spatially uniform B_1 when empty, B_1, SNR, and power deposition were highly nonuniform over the human head both at 4 and 7 T, with significantly higher nonuniformities at the higher field strength [21]. The SNR was ∼2 fold higher at 7 T versus 4 T in the *center* of the brain whereas in the periphery the SNR gain was only ∼1.4 fold [21].

The consequence of this nonuniform B_1^+ was already evident in the early 4 T images [Fig. 1(a)] and accounted for the highly nonuniform center bright image intensity and contrast degradation. It was originally ascribed to "dielectric resonances" [10], [11]. However, as shown in [32] (see Fig. 2) such resonances are not sustained in the ionic environment of human tissues but could arise from the complex interaction of the traveling waves associated with each current carrying element of the coil. This was confirmed using both modeling and experiments [33], exploiting multichannel transmit technology and coils introduced in [52]. An eight channel transmit and receive (Tx/Rx) coil was employed with the same elements being used both for transmission and reception (Fig. 3). With such a coil, it was possible to transmit with one element and receive with all the elements in this multichannel Tx/Rx array, thus experimentally mapping B_1^+ phase and amplitude of each individual element and reconstructing B_1^+ either for the circularly polarized (CP) mode of a conventional transmitter [Fig. 3(a)] or using other constructs [Fig. 3(b)].

The B_1^+ pattern from a *single element* of the multichannel transmit coil shown in Fig. 3 is spatially nonuniform, not only in amplitude, but, much more importantly and remarkably so, in *phase* [33] as expected from the traveling wave nature of the RF at this magnetic field strength.

When the transmission is in the CP mode, the *vector (*i.e., *complex)* addition of B_1^+ produced by each element is constructive in some places (e.g., the center of the head) or leads to

partial cancellation in others, resulting in a "volume coil" transmit B_1 amplitude pattern shown in Fig. 3(a) [33]. If we approximate where the human head boundaries would be and superimpose it on this pattern [white line in Fig. 3(a)], we would see in the human head the well known, center bright transmit B_1 profile, as documented at 4 and 7 T in [21]. If, on the other hand, we transmit with each element individually and form a construct based on B_1^+ *magnitudes* alone, analogous to what can be done for multichannel receive operation, then the pattern is no longer center bright [Fig. 3(b)] [33]; on the contrary, it is weak in the center and strong in the periphery.

Of course, in practice, in the CP *transmission* mode, a "vector" addition of B_1^+ from each current carrying element is accomplished in hardware during the pulse. It would be impractical to pulse each element one at a time and then generate a magnitude combination as in Fig. 3(b). Therefore, one normally operates under conditions of Fig. 3(a), with destructive interferences leading to relatively lower flip angles in the periphery of the human head. These destructive interferences, which become more pronounced at higher fields, are the source of less than linear SNR gains in the periphery of the brain when using a volume transmit and receive coil [21]. When such interferences are avoided, as in single voxel spectroscopy executed using small voxels, SNR gains in the periphery also increase slightly better than linearly in going from 4 to 7 T [39].

The B_1^+ inhomogeneity problem can be ameliorated or corrected using multichannel transmit coils and parallel transmit capability [48], [52], [53] together with various strategies such as B_1-shimming [49], [50], [52]–[55], transmit sense (e.g., [56]–[58]), spoke pulses (e.g., [59]–[65]), k T pulses [66], etc., to generate uniform flip angles over a targeted region such as the brain. The detected signal intensity will still be nonuniform due to the spatially inhomogeneous sensitivity of the receive coil(s). However, "destructive interferences" *per se* can be avoided or minimized on the receive side if a multichannel receive coil is employed with signals for each channel collected separately but simultaneously and only combined subsequently.

The SNR increases measured at 7 T relative to 4 T [21] were for same bandwidth and full relaxation. Such conditions are not universally applicable in image acquisition. With repetitive RF pulsing without full relaxation, SNR will be diminished but more so at higher fields for nuclear spins such as protons, where spin-lattice relaxation times get longer with increasing magnetic fields ([67] and references therein). Other nuclei such as ^{17} O and ^{31}P [30], [68] will be unaffected or even gain due to this phenomenon. Similarly, under many conditions, the bandwidth needs to be higher at the higher field strength, leading the noise increase as the square root of the bandwidth.

SNR gains with increasing magnetic fields can be larger with low gyromagnetic nuclei such as ^{17} O, ^{23}Na, ^{13} C, and ^{31}P all of which are of great biological interest. Among these nuclei, ^{17}O and ^{23}Na resonate at particularly low frequencies. For example, at 9.4 T, ^{17}O resonates at 54 MHz while the ^{1}H resonance frequency is 400 MHz. At such low frequencies, SNR can vary with magnetic field according to $B_o^{7/4}$ [69], [70] even in conductive biological samples. Consistent with theory, approximate quadratic dependence of

SNR on field strength was experimentally observed between 9.4 and 4.7 T in the rat brain [68] for direct detection of the ^{17}O nucleus. This sensitivity gain was critical in performing biologically important measurement of oxygen consumption rate in the brain (e.g., [40], [71]). For these low gyromagnetic nuclei, going to fields higher than 7 T, such as 10.5 or 11.7 T that are expected to be operational soon will bring significant SNR gains, hence spatial and/or temporal resolution.

IV. Functional Neuroimaging

A. Imaging Brain Function During a Stimulus or Performance of a Task

fMRI has rapidly emerged as the dominant and virtually indispensable method for studying the human brain, which is endowed with unique capabilities that often cannot be studied in animal models. Since its introduction in 1992 [14], [15], [72], fMRI has fueled explosive developments in the investigation of brain function, achieving depiction of functional activity in three dimensions from whole brain studies with approximately a millimeter resolution to imaging with submillimeter resolution at the level of cortical columns [73]–[81], layers, [82]–[85] and other fine scale organizations, such as frequency preference in the human inferior colliculus [86], and digits of the hand [87], [88]. Functional mapping of such fine scale organizations has been possible only at high and ultra high fields. Orientation columns, which were never previously depicted in the human brain, were imaged at 7 T for the first time together with ocular dominance columns (ODCs), revealing the organizational relationship between them [74] (see Fig. 4). This was possible only with ultrahigh magnetic fields and extensive theoretical and experimental studies aimed at understanding the complex set of mechanisms underlying the ultimate coupling between neuronal activity and MRI signals. Demonstrating the feasibility of obtaining functional maps of such columnar organizations heralded the exciting prospect of exploring unmapped and/or unknown functional organizations in the human brain at the level of elementary computational units.

In addition to the indispensable improvements in spatial accuracy, SNR, and functional contrast-to-noise ratio (fCNR) to achieve some of the most advanced applications of fMRI, ultra-high fields have in fact provided one of the most, if not the most, important tool to study the mechanisms operative in fMRI.

Functional imaging signals predominantly originate from the BOLD (blood oxygenation level dependent) mechanism [16]; this mechanism relies on the magnetic susceptibility difference between intravascular space containing deoxyhemoglobin and surrounding tissue and, as such, is amplified with magnetic field magnitude (e.g., [16], [17], [89], [90]). These early BOLD models are largely accurate, albeit incomplete with respect to definition of the fMRI signals. Some of the contributions that were unaccounted for in the early modeling efforts, such as intravascular BOLD [20], [29], [91] and inflow effects [92]–[94] form the basis for the successful use of lower field magnets, such as 1.5 T, for the acquisition of functional images.

Nevertheless, a more comprehensive understanding of the origins of fMRI signals ([20] and references therein) have also reconfirmed our initial expectations that ultrahigh fields provide major advantages for high resolution and high accuracy functional mapping; these

expectations have been largely demonstrated experimentally by a plethora of studies conducted with high magnetic fields (e.g., see reviews [95]–[99]). However, some of the gains tend to level off with increasing field magnitude [20].

One of the major advantages of ultrahigh fields is increased spatial accuracy of fMRI signals. The dominant approach employed in fMRI applications is T_2^* weighted gradient recalled echo (GRE) fMRI technique, implemented with echo planar imaging (EPI)-based acquisition. GRE fMRI, however, suffers from spatial inaccuracies in functional mapping because of large vein contributions. Often one is concerned with the large blood vessels on the pial surface of the brain. This major confound was realized and documented as early as in 1993 [100], [101] and was recently further reemphasized [84].

GRE fMRI studies would also have a strong contribution from ∼50 to ∼100 μ diameter intracortical veins that run perpendicular to the cortical surface and drain the different layers. These are the veins that were visualized in the original BOLD imaging work conducted in rats [102]; they can also be seen in very high-resolution human brain images with high T_2^* or phase contrast (e.g., [53], [103], [104]). These intracortical small veins can be limiting to laminar specific studies [105]–[107] but they would certainly produce functional mapping signals more accurate than the draining pial veins.

In GRE fMRI, the BOLD effect comes from *extravascular* and *intravascular* sources. The latter originates from the T_2 and T_2^* changes accompanying the stimulus- or task-induced alterations in deoxyhemoglobin content in blood and occurs at all levels of the vasculature; hence, it can degrade the spatial fidelity of fMRI maps. But this confound is diminished at ultrahigh fields as blood T_2 and, more relevantly for GRE fMRI, blood T_2^* decreases [20], [29] and becomes much shorter than tissue values of this parameter. Consequently, in a typical GRE fMRI acquisition where echo time TE is set approximately equal to tissue T_2^*, blood contribution to the image can be significantly reduced or even absent depending on the field strength [29]. This suppresses or even eliminates one of the major contributions to inaccurate functional signals, one associated with the intravascular blood effect.

Unlike the *intravascular* BOLD contribution, however, the *extravascular* BOLD effect persists at all field strengths and increases with increasing field magnitude [20]; because of this, large draining veins continue to be a source of inaccurate functional mapping signals in GRE fMRI even at ultrahigh fields. However, the microvascular contributions to functional mapping signals originating from capillaries, postcapillary venules, and intracortical small veins also get significantly larger at the ultrahigh fields due to both extra- and intravascular BOLD mechanisms [22], [108], enabling accurate mapping that would not be possible at lower magnetic fields. This relative microvascular gain was demonstrated in early 7 T studies [22], [109]. Recently, the presence of this microvascular contribution at 7 T was relied upon when it was demonstrated that, in high resolution 7 T fMRI studies, “stripping” away the outer cortical layers where the pial vein contribution is dominant and looking into deeper layers of the cortex [84] yielded more accurate functional maps. Without the significant presence of the functional mapping signals of microvascular origin in addition to the large pial vessel effects on the cortical surface, this strategy would not have worked.

The low-fidelity large vessel effects that persist in GRE fMRI even at high fields can be suppressed with spin echo (SE)-based fMRI at ultrahigh but *not* at low magnetic fields. SE fMRI responds to apparent T_2 (as opposed to T_2^*) changes both in the extravascular space around microvasculature (capillaries and small postcapillary venules) and in blood itself [20], [91], [95], [110]. Functional mapping signals associated with extravascular component of the SE mechanism are expected to provide improved spatial specificity. The intravascular T_2 effect, on the other hand, is associated with all deoxyhemoglobin containing blood vessels, large and small; hence, it can degrade spatial specificity of functional maps due to the large vessels exhibiting intravascular T_2 changes. Fortuitously, the blood T_2 becomes significantly smaller than brain tissue T_2 at ultrahigh fields, as previously mentioned, ([20], [29] and references there in) so that at TE values that correspond approximately to gray matter T_2, the blood signal would be significantly diminished, and even undetectable.

At 3 T, ∼50% of the SE fMRI signals were shown to arise from blood [111]. But at 7 T, the blood contribution was estimated to be less than 10% at echo times matching gray matter T_2 [29]. Consequently, at very high fields such as 7 T or higher, the functionally *nonspecific* blood component and the extravascular BOLD effect associated with large veins are both suppressed in SE studies [20], [29], [109]. Residual large vessel effects are still expected because the extravascular BOLD effect with large blood vessels is not exactly zero in SE fMRI; rather, it is small and significantly less than effects associated with microvasculature [20].

When viewing SE fMRI data, however, one must remember that SE-based fast sequences most frequently used for fMRI do not encode pure spin echo contrast; rather, they contain T_2^* “contaminations” the extent of which depend on specific acquisition parameters.

The advantages of high and ultrahigh field fMRI have largely been exploited in applications where a section of the brain, such as the primary visual cortex (e.g., [73], [74], [112], area MT [80] or the auditory cortex (e.g., [25], [85], [86]) was studied using field of view restriction. Ultimately, however, we need to cover the entire brain in high resolution. Only recently, significant progress has been made in tackling the difficulties inherent in obtaining rapid whole brain coverage at 7 T using techniques like GRE EPI, the predominant method employed in fMRI.

EPI (or similar fast acquisition techniques such as those based on spiral trajectories) are challenged by the shorter T_2^* and increased magnetic field inhomogeneities at high fields. The problem is particularly severe for “single-shot” techniques that acquire the entire desired *k*-space in a single echo train after the RF pulse. Higher resolution imaging, enabled by the increased SNR of the ultrahigh fields, exacerbates the problem as the echo train length is elongated with the increased spatial resolution. However, such single-shot methods are critically important in fMRI; replacing them with multishot, segmented versions prolongs acquisition times, and more importantly, increases temporal signal variations (i.e., temporal SNR) in the fMRI time series, and hence degrades fCNR of the activity maps.

The transformative technology that alleviated the afore-described problem is parallel imaging to undersample the phase encode direction [113]–[115]. In EPI, the use of parallel

imaging allows the echo train length to be shorter by skipping k-space lines. This minimizes phase accrual due to off-resonance effects, thus decreasing distortions and reducing signal loss due to T_2^* decay during the echo train. GRE EPI-based fMRI images with diminished distortion artifacts were demonstrated shortly after the introduction of parallel imaging (e.g., [116], [117]). At the present, it is possible to obtain excellent submillimeter isotropic resolution, slice selective GRE EPI images over the entire brain at 7 T with a 32-channel receive coil using parallel imaging with a reduction factor (and maximum aliasing) of 4 along the phase encode direction; such images (e.g., see Fig. 2 in [118] and Fig. 5 in this paper) provide an excellent basis for ultrahigh field and ultrahigh resolution fMRI studies. In 3-D EPI with two phase encode directions, even higher 2-D reduction factors can be attained [119], decreasing both the echo train length as well as the 3-D volume acquisition times significantly.

Parallel imaging is also highly synergistic with ultrahigh fields. Complex phase patterns generated over the object by the traveling wave behavior of the RF at higher fields, discussed before, help suppress spatially dependent noise amplification (i.e., g-factor noise [114]) for a given size object [120]–[123]. Of course, reducing the number of *k*-space lines collected decreases the SNR by the square root of the reduction factor. However, the consequences of this reduction are less significant at higher fields where there are inherent SNR gains. In particular for fMRI, reduction in the SNR of each individual image in the fMRI time series does not determine fCNR unless temporal signal variance is dominated by thermal noise (e.g., [108], [124]–[129] and references therein); this is often not the case except for very high resolution imaging. The use of parallel imaging can even improve the fCNR despite the loss of SNR in each image of the fMRI time series, for example, by avoiding segmentation [128].

Of course, high resolution whole brain coverage also leads to increased volume acquisition times (TR) necessitating compromises such as thick slices, large interslice gaps or sacrificed temporal resolution (e.g., [119], [130]–[135]).

Motivated by the prospect of acquiring high resolution, whole brain fMRI data at 7 T, but confronted with the long TRs required for whole brain coverage, “slice accelerated” multiband (MB) imaging, also referred to as simultaneous multislice (SMS) imaging, was introduced for GRE fMRI using concurrent accelerations along both the slice and in-plane phase-encode directions [136], [137]. In this approach, several slices are simultaneously excited using multibanded RF pulses and subsequently acquired in a single EPI echo train; the simultaneously acquired slices are then unaliased using parallel imaging principles.

The performance of the MB approach is significantly improved by effectively shifting the simultaneously excited and acquired slices relative to each other in the phase encoding direction [118], [138]–[141]. An example of whole brain 7 T GRE EPI images, of the type that would be used for fMRI studies, acquired with the multiband acceleration and 1-mm isotropic resolution is illustrated in Fig. 5.

Multiband EPI acquisitions at 7 T, especially when high-resolution imaging is desired, must employ “in-plane” parallel imaging with phase encode undersampling in addition to

acceleration along the slice direction. This is not necessarily the case at lower fields. The data in Fig. 5, for example, employed a MB acceleration of 4 and in-plane acceleration of 3, thus achieving a 12-fold 2-D acceleration. The original 7 T work with Multiband reported a 16-fold 2-D acceleration [136], [137]. However, the use of phase encode undersampling inevitably reduces the maximum achievable slice acceleration since both processes rely on the same coil-specific spatial information.

Especially at 7 T, but even at lower fields strengths such as 3 T, the multiband technique quickly runs in to peak power and power deposition limitations, particularly when employed with spin echoes as in diffusion-weighted imaging. Efforts based on using different RF pulses [142], [143] or parallel transmit pulse design [64], [118] has been important advances to overcome these limitations. The parallel transmit pulse design approach provides the unique capability to improve the flip angle distribution over the targeted volume while constraining power parameters [64], [118]; this has been demonstrated first for total RF power [64], [118] and recently extended to global and local power deposition [144]–[146].

Although these slice accelerated sequences have been introduced for fMRI initially at 7 T [136], [137], they have so far been employed at 3 T predominantly within the context of the Human Connectome Project for resting state and task fMRI, and diffusion imaging for tractography [118], [147]–[152]. However, these techniques clearly will enable high resolution whole brain imaging rapidly at all field strengths and will find numerous applications in high resolution fMRI studies at ultrahigh fields.

B. Resting State Networks

Resting state functional magnetic resonance imaging (rfMRI) uses correlations in the spontaneous temporal fluctuations in an fMRI time series to deduce “*functional connectivity*”; it serves as an indirect but nonetheless invaluable indicator of gray-matter regions that interact strongly and, in many cases, are connected anatomically (e.g., see [150] and references therein).

Resting state does not refer to the brain being at rest, which is never the case; rather it simply refers to the subject being at “rest” in the scanner, not performing a directed task or exposed to an external stimulus as in normal fMRI. An fMRI time series collected in such a state contains fluctuations that often display strong correlations among distant gray matter regions, revealing networks of interconnected temporal variations, referred to as resting state networks (RSNs). These correlated fluctuations are thought to largely reflect spontaneous neural activity [131], [153]–[155]. However, it remains unclear why functionally related areas undergo such spontaneous fluctuations. As would be expected, the spontaneous activity detected in resting state fMRI signals are as much as 2 fold larger at 7 T compared to 3 T under similar data acquisition conditions [131]; this field dependence can be exploited to obtain resting state data at higher spatial resolution and/or without having to perform intersubject averaging [156].

Detailed studies of RSNs with rfMRI have been restricted to 3 T or lower magnetic fields. At 3 T, rfMRI experiments typically use voxel volumes of approximately 27 mm^3 (i.e., 3-mm isotropic voxels) to achieve sufficient minimum SNR and fCNR. Furthermore,

typically, these studies employ spatial smoothing with large Gaussian kernels [∼4 to 6 mm FWHM (full width at half maximum)] to reduce noise, and often also resort to group averaging, which further amplifies spatial blurring by requiring additional smoothing (∼6–8 mm FWHM) of the functional data to compensate for the variability of anatomical structures across subjects. Consequently, at 3 T, the “partial volume” effects arising from the large effective voxel volume employed as well as the nonspecific spread of the activation [109] constrain the spatial accuracy of the resulting rfMRI maps.

The exception to the very large voxel sizes typically employed at 3 T are the recent data generated within the human connectome project (HCP) [149] where the voxel size for the rfMRI data is 2 mm isotropic [118], [150]. This was feasible because of the use of slice accelerated multiband technique with an acceleration (i.e., MB factor) factor of 8, resulting in subsecond (0.7 s) whole brain coverage [118], [150]. Such rapid sampling of the spontaneous fluctuations in an rfMRI time series was shown to improve the statistical significance of the resulting RSNs detected [150], [157]; in the HCP, this was further confirmed, resulting in previously unobtainable number of independent and highly fine grained RSNs [150] as well as remarkable correlation with phenotypes [158].

The higher functional specificity, and fCNR inherent at ultrahigh fields such as 7 T can be exploited to further alleviate the limitation on either the number of independent RSNs detected and/or the spatial resolution of the RSNs. However, ultrahigh field efforts have been focused on rfMRI only recently. A high resolution examination of RSNs conducted at 7 T [156] demonstrated the detection of spontaneous fluctuations within functionally connected networks in single subjects without the need for spatial smoothing, at nominal voxel volumes as small as 1 mm^3 (isotropic voxel dimension), significantly smaller than the voxel sizes employed at 3 T. An example from this 7 T work is illustrated in Fig. 6. The areas in color are regions that show distinct correlated spontaneous fluctuations and, as such, are consider functionally related.

So far, these 7 T rfMRI studies, however, were not performed with the previously mentioned slice-accelerated multiband sequences that improve the statistical significance of RSNs detected. Additional gains will definitely be realized with slice-accelerated sequences as indicated by the piloting efforts actively pursued currently within the human connectome project [118].

V. Structural Neuroimaging

Structural MRI is increasingly accepted as a surrogate for anatomic phenotype. It is not hard to find examples where anatomic MRI has transformed the entire research landscape of a biomedical field: cerebro-vascular disease, epilepsy, multiple sclerosis, and other inflammatory conditions, cerebral developmental disorders, to some extent psychiatric disorders, and neurodegenerative disorders. Ultrahigh field MRI is anticipated to expand these boundaries and usher in new possibilities in visualizing pathologies in human diseases as well. This expectation is based on the realization that beyond the well-established SNR gains, ultrahigh fields provide significant gains in contrast mechanisms and contrast

magnitude for structural MRI. This was not necessarily predicted at the launch of the high field effort with 4 T systems, but has proven to be the case.

Morphological images of brain tissue rely largely on proton density T_1 and T_2 differences between tissue type and regional variations (e.g., white matter versus gray matter, cortex versus subcortical nuclei, etc.). Proton density is clearly a magnetic field-independent parameter. However, relaxation times T_1 and T_2 are field dependent, with T_1 generally increasing and the T_2 and T_2^* decreasing with field strength (see review [159] and data compiled from the literature in [20]). What was surprising was that, contrary to expectations, the *dispersion* in T_1 also increases with increasing magnetic fields in the brain, leading to superior T_1-weighted structural images at the higher magnetic fields [67]. This superior T_1 contrast was in fact observed in the early 4 T anatomical images; at 4 T, white matter was noted to be no longer uniform in appearance as in 1.5 T and that previously unseen white matter structures, such as the optic radiation, were clearly visualized [12], [13].

It is not known if, as in the case of T_1, the dispersion of the T_2 values in the brain also increases with higher magnetic fields. T_2-based contrast-to-noise ratio nevertheless benefits at least from the SNR gains at ultrahigh fields. Combined with high resolutions that can be attained, T_2 weighted images at 7 T have yielded unprecedented anatomical detail. For example, T_2 weighted high resolution images at 7 T provided exquisite anatomy of the hippocampus (Fig. 7), permitting segmentation of the subcompartments of the hippocampus, visualization of the internal structures of malrotated hippocampal bodies, and the paucity of interdigitations in patients with temporal lobe epilepsy (TLE) [160].

At high magnetic fields, other unique contrast mechanisms that are not typically employed at lower field strengths (or not employed with equal success) have emerged as well. These are T_2^* weighted imaging, phase imaging, susceptibility imaging, and susceptibility weighted imaging (SWI).

The T_2^* weighted imaging can be obtained in a straightforward fashion simply using gradient recalled echoes; it exploits the fact that T_2^* of a given voxel gets influenced by tissue specific processes, such as microscopic susceptibility differences, and the fact that field inhomogeneities induced by susceptibility differences are proportional to the magnetic field magnitude. At the high resolutions attainable with ultrahigh fields, this simple approach was shown to yield exquisite brain anatomy, for example, at 8 T in the very early days of ultrahigh field imaging ([34] and references therein).

SWI [161] also relies on susceptibility differences and emphasizes the contrast in the magnitude images by multiplication with a mask obtained from the phase of the same data; it has produced remarkable anatomical detail at 7 (e.g., [162] and 9.4 T [103]). Fig. 8 displays SWI images depicting venous blood vessels obtained at 3 and 9.4 T [103]. These blood vessels are visible in SWI data because of the strong susceptibility difference between the vessel interior and surrounding tissue, induced by the presence of the strongly paramagnetic deoxyhemoglobin molecule in the venous side of the circulation. Based on this capability, it would be expected, for example, that microbleeds (a problem of clinical

concern) can be detected better at the 7 T or higher magnetic fields (e.g., [163]–[165]) compared to the clinically used fields of 1.5 and 3 T.

Phase imaging was introduced using 7 T [166], [167] and exploits the fact that there exists frequency differences between gray and white matter and many other structures of the brain. Thus, the phase of the MR signal in the brain disperses as a result of this frequency difference and can be mapped. The origin of this frequency difference is still discussed in the literature (e.g., [168]–[173]) and largely appears to reflect iron and/or myelin content; however, the fact that it can generate images with exquisite anatomical detail is unquestioned.

The aforediscussed contrast mechanism all represent in part, if not fully, different ways of detecting the consequences of susceptibility heterogeneities. Rather than these indirect measurements, direct quantitative susceptibility mapping has also emerged as a way of reproducibly imaging the intrinsic tissue susceptibility contrast, which at ultrahigh fields such as 7 T produce images that contain detailed anatomical information (e.g., [174]–[176]).

One of the clear gains for morphological imaging at ultrahigh fields is vascular imaging *without* the use of exogenous contrast agents. Such a capability is of paramount importance for a variety of fields, including for fMRI mechanisms [177] where vasculature plays a critical role in coupling physiological events to MR detectable signals, tumor biology where angiogenesis is necessary for tumor growth and, of course, in clinical medicine where ischemic events due to blood vessel occlusion are cause of pathologies. Time-of-flight (TOF) methods employed for imaging vasculature without exogenous contrast benefit from both the enhanced SNR and the long T_1 of ultrahigh fields. Blood T_1 is virtually insensitive to its oxygenation state and also increases linearly with field strength going from 1.5 to 9.4 T according to $T_1 = 1.226 + 0.134B_0$ [178]. Prolongation of tissue T_1 permits improved background suppression in TOF angiography. The combined effects impart a clear benefit in TOF imaging of vasculature on the arterial side [55], [179]–[181], as well as in perfusion imaging using spin-labeling techniques. Small diameter arterial blood vessels that are poorly visualized or undetected at 3 T can be clearly seen at 7 T TOF angiography, without the use of any exogenous contrast agent, especially when using techniques that overcome the power deposition and B_1 nonuniformity limitations [55], [181] of ultrahigh magnetic fields (Fig. 9).

VI. Imaging in the Human Torso

Ever since the discouraging early 4 T results from Siemens laboratories [11], and similar unpublished results from the other two major manufacturers, the human torso has been considered too difficult to tackle at ultrahigh fields. Consequently, work carried out at 4 T and higher magnetic fields have been restricted predominantly to the head or the extremities [5] and breast [182] where the object size relative to the RF wavelength employed is manageable. In the torso, the exception was imaging the prostate but with a small endorectal coil positioned immediately adjacent to the tissue of interest [51], [182].

Fig. 10(a) shows an image of a single slice through the body obtained at 4 T in early work [11], and indeed it highlights the presence of major problems. As previously discussed, these problems were ascribed to a “dielectric resonance” at the time. However, again, as already

discussed, this problem is now understood to arise from the smaller wavelength of the RF relative to the object size, leading to a damped traveling wave behavior [32], and consequently, to large and spatially rapid phase variations over the object; the rapidly varying phase in return results in destructive interferences producing areas of diminished transmit and receive B_1 amplitudes and hence nonuniform signal intensity and SNR [33].

The ability to manipulate the transmit RF is ultimately necessary to overcome the aforedescribed problem and perform imaging in the human torso at ultrahigh fields. Our solution to this problem was the use of multichannel transmitters with channel specific independent control [48], [52], [53]. There is often the misconception that using the Faraday shield of the gradient set as a cavity and a patch antenna to drive it [183], the so-called "traveling wave MR," would lead to a uniform B_1^+ field and spin excitation in the entire human body. However, from the cavity, the RF must still "penetrate" into and travel within the human body in the transverse direction and these traveling waves within the body still create destructive interferences and, therefore, nonuniformities. Thus, the patch antenna excitation must also have the means to shape the B_1^+ within the human torso, as in the multichannel transmit approach, for it to be ultimately useful in human torso imaging at ultrahigh fields.

With the multichannel approach, particularly combined with local transmit coil arrays placed in close proximity to the torso, B_1^+ fields can be maximized and/or homogenized over a predetermined region, enabling imaging of targeted organs in the human torso at 7 T for the first time [48]–[50], [54], [65], [184]–[186]. Fig. 10(b) illustrates that the problems that resulted in the poor torso images at 4 T have been solved using multichannel transmit methodology combined with local transmit arrays even at 7 T, yielding exquisite cardiac anatomy, the organ targeted in this study [49], [185]. Fig. 10(c) and (d) shows B_1^+ maps in a slice as in Fig. 10(b), demonstrating that normally the B_1^+ maps are inhomogeneous and also very weak [Fig. 10(c)] over the targeted organ, the heart [49], [185]. However, with B_1^+ shimming techniques, RF uniformity and magnitude are improved over the target [Fig. 10(d)], leading to 7 T images of the type illustrated in Fig. 10(b).

Since the original work from our laboratory for body imaging [48]–[50], imaging in the human torso using multichannel parallel transmit techniques and local multichannel transmit and receive array coils have been adapted and utilized for human torso studies by other groups as well (e.g., [4], [187]–[198]) and is a growing endeavor. These efforts have resulted in diverse coil geometries (e.g., [4], [48]). Significant further developments in this area are expected, including larger number of transmit and receive coils, advanced pulse designs such as multispoke pulses for improved B_1^+ homogeneity, and significantly higher accelerations in image acquisition times through the use of multiband technique for simultaneous slice excitation and *k*-space undersampling in the phase encode direction(s). Interesting extensions of the B_1 shimming (i.e., one spoke) approach where two time-interleaved images are acquired using a different excitation mode for each to form virtual receive elements (TIAMO technique) have been shown to significantly improve homogeneity [188]. Two-spoke pulses have been employed with 16 channel transmitters

yielding significant improvements in spatial homogeneity of contrast and signal intensity over the heart [65]; similarly, using the principles described in [64], cardiac imaging with slice acceleration with parallel transmit multiband pulses to optimize B_1^+ with a power parameter regularization has been demonstrated [199]. Substantial new improvements in such techniques are expected in the future.

An area where ultrahigh fields are bound to be extremely beneficial in the torso, as in the brain, is angiography and perfusion imaging of organs like the heart and kidney using endogenous contrast. Excellent angiography of kidney arterial blood vessels was demonstrated using endogenous TOF contrast at 7 T [184].

VII. SAR Challenge

One of the most significant challenges facing ultrahigh fields is SAR (Specific Absorption Rate), i.e., the power deposited into the subject. SAR increases supralinearly with increasing magnetic fields due to the correspondingly higher frequency RF that must be employed, and becomes even more complex when multichannel parallel transmit (pTx) technology is engaged to solve ultrahigh field B_1^+ problems.

Regulatory bodies, such as the FDA in the USA, set limits for “global” and “local” SAR. Even though appropriateness of these limits and the science behind them are topics of ongoing debate, they are the guidelines that define safe operating conditions.

Global SAR can be experimentally estimated, and all MRI scanners are equipped with hardware and software to do so. There are imaging applications, such as GRE-based fMRI, that are intrinsically very low in global power deposition and can run without encountering global SAR limits even at 7 T. But many other techniques, such as spin-echo-based acquisitions for diffusion weighted imaging, spin echo fMRI, anatomical imaging with “Turbo Spin Echoes,” etc., quickly run into limitations, particularly when multiband accelerations are employed.

The greater problem at ultrahigh fields is *local* SAR. This is especially of concern with pTx applications (although the solution to the problem is also pTx pulse design as discussed below). There is currently no practical way of measuring local SAR experimentally. It can be calculated by electromagnetic modeling for a given coil and an anatomical human model that occupies the coil; this approach has been extensively used, including in the very first 7 T head [21] and body [48]–[50] papers.

In a clinical scanner with a single channel transmit coil, electromagnetic simulations of a specific coil loaded with different anatomical human models are employed to establish a correlation between global SAR and local SAR for that coil. This correlation, including a safety margin that accounts for possible variations among individuals, is then employed to abide by global and local SAR limits based on the experimental measurement of global SAR alone. However, this approach completely fails for pTx. In a pTx application, amplitudes and phases of the different current carrying elements (i.e., the different transmit channels) no longer have a hardware-fixed relationship as they do in a single transmit coil setup; instead

they are now uniquely determined based on the B_1^+ maps obtained on each individual subject, the targeted region to be imaged, and the pTx RF solution employed.

Therefore, ideally, the pTx approach requires calculation of local SAR for each individual subject and for the pTx RF solution sought. Currently, this is far from being feasible within the time dictated by constraints of an MR imaging session. Consequently, one must rely on generic models. Solutions have been proposed based on evaluation of multiple models and techniques for a given coil configuration to set safety margins or employ a library of models to estimate optimal matches (e.g., [200]–[202] and references therein).

While pTx technology introduces complications with respect to local SAR, it also provides a solution for the SAR imposed limitations on power demanding imaging methods [50], [61], [64], [203]–[208]; this solution is in principle applicable to any field strength though its utmost utility is at ultrahigh fields.

Most frequently employed strategy in pTx pulse design targets a desired spatial pattern of B_1^+ (e.g., uniform flip angle over a predetermined target) and searches for a solution in the presence of a power related penalty term, such as local or global SAR or total RF energy contained the pulse. This procedure typically generates an “L-curve” that describes the performance of the pulse with respect to the targeted performance (e.g., B_1^+ uniformity) *versus* the regularized power parameter. Such an L curve is illustrated in Fig. 11 for a Multiband RF pulse design for 7 T brain imaging using a 16 channel parallel transmit coil [64]. The crossing between the horizontal and vertical dashed lines, labeled “Same fidelity” and “Same energy,” identify the performance of the same coil operated in a CP mode. At the same RMSE as the CP mode, the RF energy of the pulse is reduced significantly (∼60% for the same flip angle). The best compromise is where the L-shaped curve has an elbow, indicated by the arrow (see Fig. 11).

When solutions such as the one shown in Fig. 11 are calculated simultaneously for multiple slices, either in the context of simultaneous excitation of multiple slices with a multiband pulse [145] or sequential excitation of slices for slice selective volume coverage [209], the algorithm can minimize the local SAR by distributing the “hot-spots” to a different location for each excited slice. Consequently, hot-spots are not focused and do not add up, thus minimizing local SAR.

Solutions have also been proposed to *simultaneously* constrain more than one power parameter [208]. However, all of these elegant pTx solutions to SAR challenges still must be calculated using a human model rather than on an individual subject basis and implemented with a safety margin to account for subject variability. This, of course, sacrifices performance.

VIII. Conclusion

In the last three decades, we have witnessed major advances and refinements in techniques and instrumentation for ultrahigh magnetic fields. The introduction of commercial ultrahigh field instruments of ever increasing sophistication and robustness, and the incessant pace of

developments in image acquisition and reconstruction methods have propelled ultrahigh field MR imaging to new levels of biological information content. These advances are sure to continue unabated for years to come as the incessant creativity of the MR community produce new capabilities and overcome impediments. As new instruments like the 10.5 T system expected at the University of Minnesota and the 11.7 T systems planned for the Intramural Research division of NIH and NeuroSpin Laboratory in France come online, further advances are expected.

With the introduction of highly sophisticated commercial instruments, utility of 7 T in clinical practice is also being considered; such discussions often invoke the concept of a “killer application” even though one would, for example, find a hard time identifying a “killer application” that propelled 3 T into the clinical arena. Nevertheless, there are numerous cases where 3 T imaging is better diagnostically than a lower field one, providing justification for its preferred utility. Similarly, there are already cases where 7 T is documented to be superior in visualizing pathology than 3 T. More importantly, clinical utility of new contrast mechanisms and measurement capabilities available at ultrahigh fields remains to be explored.

Last but not least, the solutions to challenges encountered at ultrahigh fields have been highly beneficial to lower fields employed in clinical studies. This important benefit is often not well appreciated. It is not that lower fields, such as the clinically significant field of 3 T, do not suffer from problems such as B_0 and B_1 inhomogeneities or power deposition limits. They do, but one can “sweep” such problems “under the rug” at these fields and still produce usable data. Not so at 7 T or higher fields. Yet, solutions developed for 7 T, if applied, inevitably lead to improved image quality at lower fields.

Acknowledgments

The work from the CMRR, University of Minnesota, was supported in part by the NIH under Grants P41 EB015894, 1U54MH091657 (the Human Connectome Project) from the 16 Institutes and Centers of the National Institutes of Health that support the NIH Blueprint for Neuroscience Research, and P30 NS076408.

Biography

Kamil Uğurbil received the B.A. and Ph.D. degrees in physics and chemical physics, from Columbia University, New York, New York, USA.

He currently holds the McKnight Presidential Endowed Chair Professorship in Radiology, Neurosciences, and Medicine and is the Director of CMRR at the University of Minnesota. His research focus has been the development of biological magnetic resonance imaging and spectroscopy using ultrahigh magnetic fields, with particular emphasis on neuroimaging and brain function.

References

1. van der Kolk AG, Hendrikse J, Luijten PR. Ultrahigh-field magnetic resonance imaging: The clinical potential for anatomy, pathogenesis, diagnosis, and treatment planning in brain disease. Neuroimaging Clin. N Amer. May; 2012 22(2):343–362. [PubMed: 22548936]

2. Umutlu L, Ladd ME, Forsting M, Lauenstein T. 7 Tesla MR imaging: Opportunities and challenges. Rofo. Feb; 2014 186(2):121–129. [PubMed: 23996625]
3. Niendorf T, Sodickson DK, Krombach GA, Schulz-Menger J. Toward cardiovascular MRI at 7 T: Clinical needs, technical solutions and research promises. Eur. Radiol. Dec; 2010 20(12):2806–2816. [PubMed: 20676653]
4. Niendorf T, Graessl A, Thalhammer C, Dieringer MA, Kraus O, Santoro D, Fuchs K, Hezel F, Waiczies S, Ittermann B, Winter L. Progress and promises of human cardiac magnetic resonance at ultra-high fields: a physics perspective. J. Magn. Reson. Apr.2013 229:208–222. [PubMed: 23290625]
5. Moser E, Stahlberg F, Ladd ME, Trattnig S. 7-T MR-from research to clinical applications? NMR Biomed. May; 2012 25(5):695–716. [PubMed: 22102481]
6. Moser E, Meyerspeer M, Fischmeister FP, Grabner G, Bauer H, Trattnig S. Windows on the human body—in vivo high-field magnetic resonance research and applications in medicine and psychology. Sensors (Basel). 2010; 10(6):5724–5757. [PubMed: 22219684]
7. Kraff O, Fischer A, Nagel AM, Monninghoff C, Ladd ME. MRI at 7 Tesla and above: Demonstrated and potential capabilities. J. Magn. Reson. Imag. Jan 30.2014
8. Blamire AM. The technology of MRI—The next 10 years? Brit. J. Radiol. Aug; 2008 81(968):601–617. [PubMed: 18628329]
9. Bandettini PA, Bowtell R, Jezzard P, Turner R. Ultrahigh field systems and applications at 7 T and beyond: Progress, pitfalls, and potential. Magn. Reson. Med. Feb; 2012 67(2):317–321. [PubMed: 22083719]
10. Barfuss H, Fischer H, Hentschel D, Ladebeck R, Vetter J. Wholebody MR imaging and spectroscopy with a 4-T system. Radiology. Dec; 1988 169(3):811–816. [PubMed: 3187004]
11. Barfuss H, Fischer H, Hentschel D, Ladebeck R, Oppelt A, Wittig R, Duerr W, Oppelt R. In vivo magnetic resonance imaging and spectroscopy of humans with a 4 T wholebody magnet. NMR Biomed. Feb; 1990 3(1):31–45. [PubMed: 2390452]
12. Ugurbil K, Garwood M, Ellermann J, Hendrich K, Hinke R, Hu X, Kim SG, Menon R, Merkle H, Ogawa S, Salmi R. Imaging at high magnetic fields: Initial experiences at 4 T. Magn. Reson. Quart. Dec; 1993 9(4):259–277.
13. Lee JH, Garwood M, Menon R, Adriany G, Andersen P, Truwit CL, Ugurbil K. High contrast and fast three-dimensional magnetic resonance imaging at high fields. Magn. Reson. Med. 1995; 34(3):308–312. [PubMed: 7500867]
14. Ogawa S, Tank DW, Menon R, Ellermann JM, Kim SG, Merkle H, Ugurbil K. Intrinsic signal changes accompanying sensory stimulation: Functional brain mapping with magnetic resonance imaging. Proc. Nat. Acad. Sci. USA. Jul 1; 1992 89(13):5951–5955. [PubMed: 1631079]
15. Kwong KK, Belliveau JW, Chesler DA, Goldberg IE, Weisskoff RM, Poncelet BP, Kennedy DN, Hoppel BE, Cohen MS, Turner R, Cheng H-M, Brady TJ, Rosen BR. Dynamic magnetic resonance imaging of human brain activity during primary sensory stimulation. Proc. Nat. Acad. Sci. USA. Jun 15; 1992 89(12):5675–5679. [PubMed: 1608978]
16. Ogawa S, Menon RS, Tank DW, Kim SG, Merkle H, Ellermann JM, Ugurbil K. Functional brain mapping by blood oxygenation level-dependent contrast magnetic resonance imaging. A comparison of signal characteristics with a biophysical model. Biophys. J. Mar.1993 643:803–812. [PubMed: 8386018]
17. Kennan RP, Zhong J, Gore JC. Intravascular susceptibility contrast mechanisms in tissue. Magn. Reson. Med. 1994; 31:9–31. [PubMed: 8121277]
18. Weisskoff RM, Zuo CS, Boxerman JL, Rosen BR. Microscopic susceptibility variation and transverse relaxation: Theory and experiment. Magn. Reson. Med. 1994; 31(6):601–610. [PubMed: 8057812]
19. Yablonskiy DA, Haacke EM. Theory of NMR signal behavior in magnetically inhomogeneous tissues: The static dephasing regime. Magn. Reson. Med. 1994; 32(6):749–63. [PubMed: 7869897]
20. Uludag K, Muller-Bierl B, Ugurbil K. An integrative model for neuronal activity-induced signal changes for gradient and spin echo functional imaging. Neuroimage. Oct 15; 2009 48(1):150–165. [PubMed: 19481163]

21. Vaughan JT, Garwood M, Collins CM, Liu W, DelaBarre L, Adriany G, Andersen P, Merkle H, Goebel R, Smith MB, Ugurbil K. 7 T versus 4 T: RF power, homogeneity, and signal-to-noise comparison in head images. Magn. Reson. Med. 2001 Jul; 46(1):24–30. [PubMed: 11443707]
22. Yacoub E, Shmuel A, Pfeuffer J, Van De, Moortele PF, Adriany G, Andersen P, Vaughan JT, Merkle H, Ugurbil K, Hu X. Imaging brain function in humans at 7 Tesla. Magn. Reson. Med. 2001; 45(4):588–594. [PubMed: 11283986]
23. Pfeuffer J, Adriany G, Shmuel A, Yacoub E, Van De, Moortele PF, Hu X, Ugurbil K. Perfusion-based high-resolution functional imaging in the human brain at 7 Tesla. Magn. Reson. Med. May; 2002 47(5):903–911. [PubMed: 11979569]
24. Shmuel A, Yacoub E, Pfeuffer J, Van de Moortele PF, Adriany G, Hu X, Ugurbil K. Sustained negative BOLD, blood flow and oxygen consumption response and its coupling to the positive response in the human brain. Neuron. Dec 19; 2002 36(6):1195–210. [PubMed: 12495632]
25. Formisano E, Kim DS, Di Salle F, Van de Moortele PF, Ugurbil K, Goebel R. Mirror-symmetric tonotopic maps in human primary auditory cortex. Neuron. Nov 13; 2003 40(4):859–869. [PubMed: 14622588]
26. Tkac I, Andersen P, Adriany G, Merkle H, Ugurbil K, Gruetter R. In vivo (1)H NMR spectroscopy of the human brain at 7 T. Magn. Reson. Med. 2001; 46(3):451–456. [PubMed: 11550235]
27. Terpstra M, Ugurbil K, Gruetter R. Direct in vivo measurement of human cerebral GABA concentration using MEGA-editing at 7 Tesla. Magn. Reson. Med. May; 2002 47(5):1009–1012. [PubMed: 11979581]
28. Van de Moortele PF, Pfeuffer J, Glover GH, Ugurbil K, Hu X. Respiration-induced B0 fluctuations and their spatial distribution in the human brain at 7 Tesla. Magn. Reson. Med. May; 2002 47(5): 888–895. [PubMed: 11979567]
29. Duong TQ, Yacoub E, Adriany G, Hu X, Ugurbil K, Kim SG. Microvascular BOLD contribution at 4 and 7 T in the human brain: Gradient-echo and spin-echo fMRI with suppression of blood effects. Magn. Reson. Med. Jun; 2003 49(6):1019–1027. [PubMed: 12768579]
30. Lei H, Zhu XH, Zhang XL, Ugurbil K, Chen W. In vivo 31P magnetic resonance spectroscopy of human brain at 7 T: An initial experience. Magn. Reson. Med. Feb; 2003 49(2):199–205. [PubMed: 12541238]
31. Wang J, Yang QX, Zhang X, Collins CM, Smith MB, Zhu XH, Adriany G, Ugurbil K, Chen W. Polarization of the RF field in a human head at high field: A study with a quadrature surface coil at 7.0 T. Magn. Reson. Med. Aug; 2002 48(2):362–369. [PubMed: 12210945]
32. Yang QX, Wang J, Zhang X, Collins CM, Smith MB, Liu H, Zhu XH, Vaughan JT, Ugurbil K, Chen W. Analysis of wave behavior in lossy dielectric samples at high field. Magn. Reson. Med. May; 2002 47(5):982–989. [PubMed: 11979578]
33. Van de Moortele PF, Akgun C, Adriany G, Moeller S, Ritter J, Collins CM, B.Smith M, T.Vaughan J, Ugurbil K. B(1) destructive interferences and spatial phase patterns at 7 T with a head transceiver array coil. Magn. Reson. Med. Dec; 2005 54(6):1503–1518. [PubMed: 16270333]
34. Robitaille PM, Abduljalil AM, Kangarlu A. Ultra high resolution imaging of the human head at 8 tesla: 2 K x 2 K for Y2 K. J. Comput. Assist Tomogr. 2000; 24(1):2–8. [PubMed: 10667650]
35. Mangia S, Tkac I, Logothetis NK, Gruetter R, Van de Moortele PF, Ugurbil K. Dynamics of lactate concentration and blood oxygen level-dependent effect in the human visual cortex during repeated identical stimuli. J. Neurosci. Res. Nov 15; 2007 85(15):3340–3346. [PubMed: 17526022]
36. Avdievich NI, Pan JW, Baehring JM, Spencer DD, Hetherington HP. Short echo spectroscopic imaging of the human brain at 7 T using transceiver arrays. Magn. Reson. Med. Jul; 2009 62(1): 17–25. [PubMed: 19365851]
37. Mangia S, Tkac I, Gruetter R, Van de Moortele PF, Giove F, Maraviglia B, Ugurbil K. Sensitivity of single-voxel 1 H-MRS in investigating the metabolism of the activated human visual cortex at 7 T. Magn. Reson. Imag. May; 2006 24(4):343–348.
38. Oz G, Iltis I, Hutter D, Thomas W, Bushara KO, Gomez CM. Distinct neurochemical profiles of spinocerebellar ataxias 1, 2, 6, and cerebellar multiple system atrophy. Cerebellum. Jun; 2011 10(2):208–217. [PubMed: 20838948]

39. Tkac I, Oz G, Adriany G, Ugurbil K, Gruetter R. In vivo 1 H NMR spectroscopy of the human brain at high magnetic fields: Metabolite quantification at 4 T versus 7 T. Magn. Reson. Med. Oct; 2009 62(4):868–879. [PubMed: 19591201]
40. Atkinson IC, Thulborn KR. Feasibility of mapping the tissue mass corrected bioscale of cerebral metabolic rate of oxygen consumption using 17-oxygen and 23-sodium MR imaging in a human brain at 9.4 T. Neuroimage. Jun; 2010 51(2):723–733. [PubMed: 20188194]
41. Lei H, Ugurbil K, Chen W. Measurement of unidirectional Pi to ATP flux in human visual cortex at 7 T by using in vivo 31P magnetic resonance spectroscopy. Proc. Nat. Acad. Sci. USA. Nov 25; 2003 100(24):14409–14414. [PubMed: 14612566]
42. Chen W, Zhu XH, Gruetter R, Seaquist ER, Adriany G, Ugurbil K. Study of tricarboxylic acid cycle flux changes in human visual cortex during hemifield visual stimulation using (1)H-{(13)C} MRS and fMRI. Magn. Reson. Med. 2001; 45(3):349–355. [PubMed: 11241689]
43. Kingsley-Hickman PB, Sako EY, Mohanakrishnan P, Robitaille PM, From AH, Foker JE, Ugurbil K. 31P NMR studies of ATP synthesis and hydrolysis kinetics in the intact myocardium. Biochemistry. 1987; 26(23):7501–7510. [PubMed: 3427090]
44. Kingsley-Hickman PB, Sako EY, Ugurbil K, From AH, Foker JE. 31P NMR measurement of mitochondrial uncoupling in isolated rat hearts. J. Biol. Chem. 1990; 265(3):1545–1550. [PubMed: 2136855]
45. Brown TR, Ugurbil K, Shulman RG. 31P nuclear magnetic resonance measurements of ATPase kinetics in aerobic Escherichia coli cells. Proc. Nat. Acad. Sci. USA. 1977; 74(12):5551–5553. [PubMed: 146199]
46. Hetherington HP, Chu WJ, Gonen O, Pan JW. Robust fully automated shimming of the human brain for high-field 1 H spectroscopic imaging. Magn. Reson. Med. Jul; 2006 56(1):26–33. [PubMed: 16767750]
47. Juchem C, Nixon TW, McIntyre S, Rothman DL, de Graaf RA. Magnetic field homogenization of the human prefrontal cortex with a set of localized electrical coils. Magn. Resonance Med. : Official J. Soc. Magn. Resonance Med. / Soc. Magn. Resonance Med. Jan; 2010 63(1):171–180.
48. Vaughan JT, Snyder CJ, DelaBarre LJ, Bolan PJ, Tian J, Bolinger L, Adriany G, Andersen P, Strupp J, Ugurbil K. Whole-body imaging at 7 T: Preliminary results. Magn. Reson. Med. Jan; 2009 61(1):244–248. [PubMed: 19097214]
49. Snyder CJ, DelaBarre L, Metzger GJ, Van de Moortele PF, Akgun C, Ugurbil K, Vaughan JT. Initial results of cardiac imaging at 7 Tesla. Magn. Reson. Med. Mar; 2009 61(3):517–524. [PubMed: 19097233]
50. Metzger GJ, Snyder C, Akgun C, Vaughan T, Ugurbil K, Van de Moortele PF. Local B1+ shimming for prostate imaging with transceiver arrays at 7 T based on subject-dependent transmit phase measurements. Magn. Reson. Med. Feb; 2008 59(2):396–409. [PubMed: 18228604]
51. Metzger GJ, Van de Moortele PF, Akgun C, Snyder CJ, Moeller S, Strupp J, Andersen P, Shrivastava D, Vaughan T, Ugurbil K, Adriany G. Performance of external and internal coil configurations for prostate investigations at 7 T. Magn. Reson. Med. Dec; 2010 64(6):1625–1639. [PubMed: 20740657]
52. Adriany G, Van de Moortele PF, Wiesinger F, Moeller S, Strupp JP, Andersen P, Snyder C, Zhang X, Chen W, Pruessmann KP, Boesiger P, Vaughan T, Ugurbil K. Transmit and receive transmission line arrays for 7 Tesla parallel imaging. Magn. Reson. Med. Feb; 2005 53(2):434–445. [PubMed: 15678527]
53. Vaughan T, DelaBarre L, Snyder C, Tian J, Akgun C, Shrivastava D, Liu W, Olson C, Adriany G, Strupp J, Andersen P, Gopinath A, Van de Moortele PF, Garwood M, Ugurbil K. 9.4 T human MRI: Preliminary results. Magn. Reson. Med. Dec; 2006 56(6):1274–1282. [PubMed: 17075852]
54. Suttie JJ, Delabarre L, Pitcher A, Van de Moortele PF, Dass S, Snyder CJ, Francis JM, Metzger GJ, Weale P, Ugurbil K, Neubauer S, Robson M, Vaughan T. 7 Tesla (T) human cardiovascular magnetic resonance imaging using FLASH and SSFP to assess cardiac function: validation against 1.5 T and 3 T. NMR Biomed. Jan; 2012 25(1):27–34. [PubMed: 21774009]
55. Schmitter S, Wu X, Adriany G, Auerbach EJ, Ugurbil K, Van de Moortele PF. Cerebral TOF angiography at 7 T: Impact of B1(+) shimming with a 16-channel transceiver array. Magn. Reson. Med. May 2.2013 71:966–977.

56. Zhang Z, Yip CY, Grissom W, Noll DC, Boada FE, Stenger VA. Reduction of transmitter B1 inhomogeneity with transmit SENSE slice-select pulses. Magn. Reson. Med. May; 2007 57(5): 842–847. [PubMed: 17457863]
57. Katscher U, Bornert P, van den Brink JS. Theoretical and numerical aspects of transmit SENSE. IEEE Trans. Med. Imag. Apr; 2004 23(4):520–525.
58. Katscher U, Bornert P, Leussler C, van den Brink JS. Transmit SENSE. Magn. Reson. Med. Jan; 2003 49(1):144–150. [PubMed: 12509830]
59. Ma C, Xu D, King KF, Liang ZP. Joint design of spoke trajectories and RF pulses for parallel excitation. Magn. Reson. Med. Apr; 2011 65(4):973–985. [PubMed: 21413061]
60. Jankiewicz M, Zeng H, Moore JE, Anderson AW, Avison MJ, Welch EB, Gore JC. Practical considerations for the design of sparse-spokes pulses. J. Magn. Reson. Apr; 2010 203(2):294–304. [PubMed: 20172754]
61. Cloos MA, Luong M, Ferrand G, Amadon A, Le Bihan D, Boulant N. Local SAR reduction in parallel excitation based on channel-dependent Tikhonov parameters. J. Magn. Reson. Imag. Nov; 2010 32(5):1209–1216.
62. Setsompop K, Alagappan V, Gagoski BA, Potthast A, Hebrank F, Fontius U, Schmitt F, Wald LL, Adalsteinsson E. Broadband slab selection with B1+ mitigation at 7 T via parallel spectral-spatial excitation. Magn. Reson. Med. Feb; 2009 61(2):493–500. [PubMed: 19161170]
63. Zelinski AC, Wald LL, Setsompop K, Alagappan V, Gagoski BA, Goyal VK, Adalsteinsson E. Fast slice-selective radio-frequency excitation pulses for mitigating B+1 inhomogeneity in the human brain at 7 Tesla. Magn. Reson. Med. Jun; 2008 59(6):1355–1364. [PubMed: 18506800]
64. Wu X, Schmitter S, Auerbach EJ, Moeller S, Ugurbil K, Van de Moortele PF. Simultaneous multislice multiband parallel radiofrequency excitation with independent slice-specific transmit B1 homogenization. Magn. Reson. Med. Jun 25.2013 47:903–911.
65. Schmitter S, Delabarre L, Wu X, Greiser A, Wang D, Auerbach EJ, Vaughan JT, Ugurbil K, Van de Moortele PF. Cardiac imaging at 7 Tesla: Single- and two-spoke radiofrequency pulse design with 16-channel parallel excitation. Magn. Reson. Med. Nov; 2013 70(5):1210–1219. [PubMed: 24038314]
66. Cloos MA, Boulant N, Luong M, Ferrand G, Giacomini E, Le Bihan D, Amadon A. kT-points: Short three-dimensional tailored RF pulses for flip-angle homogenization over an extended volume. Magn. Reson. Med. Jan; 2012 67(1):72–80. [PubMed: 21590724]
67. Rooney WD, Johnson G, Li X, Cohen ER, Kim SG, Ugurbil K, Springer CS Jr. Magnetic field and tissue dependencies of human brain longitudinal 1 H2 Orelaxation in vivo. Magn. Reson. Med. Feb; 2007 57(2):308–318. [PubMed: 17260370]
68. Zhu XH, Merkle H, Kwag JH, Ugurbil K, Chen W. 17 O relaxation time and NMR sensitivity of cerebral water and their field dependence. Magn. Reson. Med. 2001; 45(4):543–549. [PubMed: 11283979]
69. Hoult DI, Richards RE. The signal-to-noise ratio of the nuclear magnetic resonance phenomenon. J. Magn. Reson. 1976; 24(71):71–85.
70. Wen H, Chesnick AS, Balaban RS. The design and test of a new volume coil for high field imaging. Magn. Reson. Med. 1994; 32:492–498. [PubMed: 7997115]
71. Zhu XH, Zhang Y, Tian RX, Lei H, Zhang N, Zhang X, Merkle H, Ugurbil K, Chen W. Development of (17)O NMR approach for fast imaging of cerebral metabolic rate of oxygen in rat brain at high field. Proc. Nat. Acad. Sci. USA. Oct 1; 2002 99(20):13194–13199. [PubMed: 12242341]
72. Bandettini PA, Wong EC, Hinks RS, Tikofsky RS, Hyde JS. Time course EPI of human brain function during task activation. Magn. Reson. Med. 1992; 25(2):390–397. [PubMed: 1614324]
73. Yacoub E, Shmuel A, Logothetis N, Ugurbil K. Robust detection of ocular dominance columns in humans using Hahn Spin Echo BOLD functional MRI at 7 Tesla. Neuroimage. Oct 1; 2007 37(4): 1161–1177. [PubMed: 17702606]
74. Yacoub E, Harel N, Ugurbil K. High-field fMRI unveils orientation columns in humans. Proc. Nat. Acad. Sci. USA. Jul 29; 2008 105(30):10607–10612. [PubMed: 18641121]

75. Menon RS, Ogawa S, Strupp JP, Ugurbil K. Ocular dominance in human V1 demonstrated by functional magnetic resonance imaging. J. Neurophysiol. May; 1997 77(5):2780–2787. [PubMed: 9163392]
76. Cheng K, Waggoner RA, Tanaka K. Human ocular dominance columns as revealed by high-field functional magnetic resonance imaging. Neuron. Oct 25; 2001 32(2):359–374. [PubMed: 11684004]
77. Goodyear BG, Menon RS. Brief visual stimulation allows mapping of ocular dominance in visual cortex using fMRI. Human Brain Map. Dec; 2001 14(4):210–217.
78. Fukuda M, Moon CH, Wang P, Kim SG. Mapping isoorientation columns by contrast agent-enhanced functional magnetic resonance imaging: Reproducibility, specificity, and evaluation by optical imaging of intrinsic signal. J. Neurosci. Nov 15; 2006 26(46):11821–11832. [PubMed: 17108155]
79. Shmuel A, Chaimow D, Raddatz G, Ugurbil K, Yacoub E. Mechanisms underlying decoding at 7 T: Ocular dominance columns, broad structures, and macroscopic blood vessels in V1 convey information on the stimulated eye. Neuroimage. Feb 1; 2010 49(3):1957–1964. [PubMed: 19715765]
80. Zimmermann J, Goebel R, De Martino F, Van de Moortele PF, Feinberg D, Adriany G, Chaimow D, Shmuel A, Ugurbil K, Yacoub E. Mapping the organization of axis of motion selective features in human area MT using high-field fMRI. PLoS One. 2011; 6(12):e28716. [PubMed: 22163328]
81. Chaimow D, Yacoub E, Ugurbil K, Shmuel A. Modeling and analysis of mechanisms underlying fMRI-based decoding of information conveyed in cortical columns. Neuroimage. May 15; 2011 56(2):627–642. [PubMed: 20868757]
82. Olman CA, Harel N, Feinberg DA, He S, Zhang P, Ugurbil K, Yacoub E. Layer-specific fMRI reflects different neuronal computations at different depths in human V1. PLoS One. 2012; 7(3):e32536. [PubMed: 22448223]
83. Koopmans PJ, Barth M, Orzada S, Norris DG. Multi-echo fMRI of the cortical laminae in humans at 7 T. Neuroimage. Jun 1; 2011 56(3):1276–1285. [PubMed: 21338697]
84. Polimeni JR, Fischl B, Greve DN, Wald LL. Laminar analysis of 7 T BOLD using an imposed spatial activation pattern in human V1. Neuroimage. Oct 1; 2010 52(4):1334–1346. [PubMed: 20460157]
85. De Martino F, Zimmermann J, Muckli L, Ugurbil K, Yacoub E, Goebel R. Cortical depth dependent functional responses in humans at 7 T: Improved specificity with 3D GRASE. PLoS One. 2013; 8(3):e60514. [PubMed: 23533682]
86. De Martino F, Moerel M, Van de Moortele PF, Ugurbil K, Goebel R, Yacoub E, Formisano E. Spatial organization of frequency preference and selectivity in the human inferior colliculus. Nature Commun. Jan 22.2013 4:1–8. art. 1386.
87. Stringer EA, Chen LM, Friedman RM, Gatenby C, Gore JC. Differentiation of somatosensory cortices by high-resolution fMRI at 7 T. Neuroimage. Jan 15; 2011 54(2):1012–1020. [PubMed: 20887793]
88. Sanchez-Panchuelo RM, Francis S, Bowtell R, Schluppeck D. Mapping human somatosensory cortex in individual subjects with 7 T functional MRI. J. Neurophysiol. May; 2010 103(5):2544–2556. [PubMed: 20164393]
89. Fujita N. Extravascular contribution of blood oxygenation level-dependent signal changes: A numerical analysis based on a vascular network model. Magn. Reson. Med. Oct; 2001 46(4):723–734. [PubMed: 11590649]
90. Boxerman JL, Hamberg LM, Rosen BR, Weisskoff RM. MR contrast due to intravascular magnetic susceptiblity perturbations. Magn. Reson. Med. 1995; 34:555–556. [PubMed: 8524024]
91. van Zijl PC, Eleff SM, Ulatowski JA, Oja JM, Ulug AM, Traystman RJ, Kauppinen RA. Quantitative assessment of blood flow, blood volume and blood oxygenation effects in functional magnetic resonance imaging [see comments]. Nature Med. 1998; 4(2):159–167. [PubMed: 9461188]
92. Frahm J, Merboldt K-D, Hanicke W, Kleinschmidt A, Boecker H. Brain or vein-oxygenation or flow? On signal physiology in functional MRI of human brain activation. NMR Biomed. 1994; 7(1/2):45–53. [PubMed: 8068525]

93. Segebarth C, Belle V, Delon C, Massarelli R, Decety J, Le Bas J-F, Decorpts M, Benabid AL. Functional MRI of the human brain: Predominance of signals from extracerebral veins. NeuroReport. 1994; 5:813–816. [PubMed: 8018855]

94. Glover GH, Lemieux SK, Drangova M, Pauly JM. Decomposition of inflow and blood oxygen level-dependent (BOLD) effects with dual-echo spiral gradient-recalled echo (GRE) fMRI. Magn. Reson. Med. 1996; 35(3):299–308. [PubMed: 8699940]

95. Ugurbil K, Adriany G, Andersen P, Chen W, Gruetter R, Hu X, Merkle H, Kim DS, Kim SG, Strupp J, Zhu XH, Ogawa S. Magnetic resonance studies of brain function and neurochemistry. Annu. Rev. Biomed. Eng. 2000; 2:633–660. [PubMed: 11701526]

96. Ugurbil K, Toth L, Kim DS. How accurate is magnetic resonance imaging of brain function? Trends Neurosci. Feb; 2003 26(2):108–114. [PubMed: 12536134]

97. Ugurbil K, Adriany G, Andersen P, Chen W, Garwood M, Gruetter R, Henry PG, Kim SG, Lieu H, Tkac I, Vaughan T, Van de Moortele PF, Yacoub E, Zhu XH. Ultrahigh field magnetic resonance imaging and spectroscopy. Magn. Reson. Imag. Dec; 2003 21(10):1263–1281.

98. Ugurbil K. Imaging of brain function using deoxyhemoglobin and magnetic fields. Neural Metabolism in Vivo, Advances in Neurobiology. 2012; 4:501–545.

99. Ugurbil K. Two decades of functional imaging: From nuclear spins to cortical columns. Cognitive Critique. 2012; 4:121–186.

100. Menon RS, Ogawa S, Tank DW, Ugurbil K. 4 Tesla gradient recalled echo characteristics of photic stimulation- induced signal changes in the human primary visual cortex. Magn. Reson. Med. 1993; 30(3):380–386. [PubMed: 8412612]

101. Kim SG, Hendrich K, Hu X, Merkle H, Ugurbil K. Potential pitfalls of functional MRI using conventional gradient-recalled echo techniques. NMR Biomed. Mar; 1994 7(1/2):69–74. [PubMed: 8068528]

102. Ogawa S, Lee TM. Magnetic resonance imaging of blood vessels at high fields: In vivo and in vitro measurements and image simulation. Magn. Reson. Med. 1990; 16:9–18. [PubMed: 2255240]

103. Budde J, Shajan G, Hoffmann J, Ugurbil K, Pohmann R. Human imaging at 9.4 T using T(2) *-, phase-, and susceptibility-weighted contrast. Magn. Reson. Med. Feb; 2011 65(2):544–550. [PubMed: 20872858]

104. Budde J, Shajan G, Scheffler K, Pohmann R. Ultra-high resolution imaging of the human brain using acquisition-weighted imaging at 9.4 T. Neuroimage. Aug 15.2013 86:592–98. [PubMed: 23954486]

105. Goense JB, Logothetis NK. Laminar specificity in monkey V1 using high-resolution SE-fMRI. Magn. Reson. Imag. May; 2006 24(4):381–392.

106. Harel N, Lin J, Moeller S, Ugurbil K, Yacoub E. Combined imaging-histological study of cortical laminar specificity of fMRI signals. Neuroimage. Feb 1; 2006 29(3):879–887. [PubMed: 16194614]

107. Yu X, Glen D, Wang S, Dodd S, Hirano Y, Saad Z, Reynolds R, Silva AC, Koretsky AP. Direct imaging of macrovascular and microvascular contributions to BOLD fMRI in layers IV-V of the rat whisker-barrel cortex. Neuroimage. Jan 16; 2012 59(2):1451–1460. [PubMed: 21851857]

108. Yacoub E, Van de Moortele PF, Shmuel A, Ugurbil K. Signal and noise characteristics of Hahn SE and GE BOLD fMRI at 7 T in humans. Neuroimage. Feb 1; 2005 24(3):738–750. [PubMed: 15652309]

109. Yacoub E, Duong TQ, Van de Moortele PF, Lindquist M, Adriany G, Kim SG, Ugurbil K, Hu X. Spin-echo fMRI in humans using high spatial resolutions and high magnetic fields. Magn. Reson. Med. Apr; 2003 49(4):655–664. [PubMed: 12652536]

110. Ugurbil K, Hu X, Chen W, Zhu X-H, Kim S-G, Georgopoulos A. Functional Mapping in the human brain using high magnetic fields. Philos. Trans. R Soc. Lond. B, Biol. Sci. 1999; 354(1387):1195–1213. [PubMed: 10466146]

111. Norris DG, Zysset S, Mildner T, Wiggins CJ. An investigation of the value of spin-echo-based fMRI using a stroop color-word matching task and EPI at 3 T. Neuroimage. Mar; 2002 15(3): 719–726. [PubMed: 11848715]

112. Olman CA, Van de Moortele PF, Schumacher JF, Guy JR, Ugurbil K, Yacoub E. Retinotopic mapping with spin echo BOLD at 7 T. Magn. Reson. Imag. Nov; 2010 28(9):1258–1269.
113. Sodickson WJ, Manning DK. Simultaneous acquisition of spatial harmonics (SMASH): Fast imaging with radiofrequency coil arrays. Magn. Reson. Med. Oct; 1997 38(4):591–603. [PubMed: 9324327]
114. Pruessmann KP, Weiger M, Scheidegger MB, Boesiger P. SENSE: Sensitivity encoding for fast MRI. Magn. Reson. Med. Nov; 1999 42(5):952–962. [PubMed: 10542355]
115. Griswold MA, Jakob PM, Heidemann RM, Nittka M, Jellus V, Wang J, Kiefer B, Haase A. Generalized autocalibrating partially parallel acquisitions (GRAPPA). Magn. Reson. Med. Jun; 2002 47(6):1202–1210. [PubMed: 12111967]
116. de Zwart JA, van Gelderen P, Kellman P, Duyn JH. Application of sensitivity-encoded echo-planar imaging for blood oxygen level-dependent functional brain imaging. Magn. Reson. Med. Dec; 2002 48(6):1011–1020. [PubMed: 12465111]
117. de Zwart JA, van Gelderen P, Golay X, Ikonomidou VN, Duyn JH. Accelerated parallel imaging for functional imaging of the human brain. NMR Biomed. May; 2006 19(3):342–351. [PubMed: 16705634]
118. Ugurbil K, Xu J, Auerbach EJ, Moeller S, Vu AT, Duarte-Carvajalino JM, Lenglet C, Wu X, Schmitter S, Van de Moortele PF, Strupp J, Sapiro G, De Martino F, Wang D, Harel N, Garwood M, Chen L, Feinberg DA, Smith SM, Miller KL, Sotiropoulos SN, Jbabdi S, Andersson JL, Behrens TE, Glasser MF, Van Essen DC, Yacoub E, Consortium WU-MH. Pushing spatial and temporal resolution for functional and diffusion MRI in the human connectome project. Neuroimage. Oct 15.2013 80:80–104. [PubMed: 23702417]
119. Poser BA, Koopmans PJ, Witzel T, Wald LL, Barth M. Three dimensional echo-planar imaging at 7 Tesla. Neuroimage. May 15; 2010 51(1):261–266. [PubMed: 20139009]
120. Wiesinger F, Van de Moortele PF, Adriany G, De Zanche N, Ugurbil K, Pruessmann KP. Parallel imaging performance as a function of field strength—An experimental investigation using electrodynamic scaling. Magn. Reson. Med. Nov; 2004 52(5):953–964. [PubMed: 15508167]
121. Wiesinger F, Van de Moortele PF, Adriany G, De Zanche N, Ugurbil K, Pruessmann KP. Potential and feasibility of parallel MRI at high field. NMR Biomed. May; 2006 19(3):368–378. [PubMed: 16705638]
122. Pruessmann KP. Parallel imaging at high field strength: Synergies and joint potential. Top Magn. Reson. Imag. Aug; 2004 15(4):237–244.
123. Ohliger MA, Grant AK, Sodickson DK. Ultimate intrinsic signal-to-noise ratio for parallel MRI: Electromagnetic field considerations. Magn. Reson. Med. Nov; 2003 50(5):1018–1030. [PubMed: 14587013]
124. Hu X, Kim SG. Reduction of signal fluctuation in functional MRI using navigator echoes. Magn. Reson. Med. May; 1994 31(5):495–503. [PubMed: 8015402]
125. Hyde JS, Biswal BB, Jesmanowicz A. High-resolution fMRI using multislice partial k-space GR-EPI with cubic voxels. Magn. Re-son. Med. 2001; 46(1):114–125.
126. Kruger G, Glover GH. Physiological noise in oxygenation-sensitive magnetic resonance imaging. Magn. Reson. Med. Oct; 2001 46(4):631–637. [PubMed: 11590638]
127. Triantafyllou C, Hoge RD, Krueger G, Wiggins CJ, Potthast A, Wiggins GC, Wald LL. Comparison of physiological noise at 1.5 T, 3 T and 7 T and optimization of fMRI acquisition parameters. Neuroimage. May 15; 2005 26(1):243–250. [PubMed: 15862224]
128. Moeller S, Van de Moortele PF, Goerke U, Adriany G, Ugurbil K. Application of parallel imaging to fMRI at 7 tesla utilizing a high 1D reduction factor. Magn. Reson. Med. Jul; 2006 56(1):118–129. [PubMed: 16767760]
129. van der Zwaag W, Marques JP, Kober T, Glover G, Gruetter R, Krueger G. Temporal SNR characteristics in segmented 3D–EPI at 7 T. Magn. Reson. Med. Feb; 2012 67(2):344–352. [PubMed: 21656557]
130. Bianciardi M, Fukunaga M, van Gelderen P, Horovitz SG, de Zwart JA, Duyn JH. Modulation of spontaneous fMRI activity in human visual cortex by behavioral state. Neuroimage. Mar 1; 2009 45(1):160–168. [PubMed: 19028588]

131. Bianciardi M, Fukunaga M, van Gelderen P, Horovitz SG, de Zwart JA, Shmueli K, Duyn JH. Sources of functional magnetic resonance imaging signal fluctuations in the human brain at rest: A 7 T study. Magn. Reson. Imag. Oct; 2009 27(8):1019–1029.

132. Bianciardi M, van Gelderen P, Duyn JH, Fukunaga M, de Zwart JA. Making the most of fMRI at 7 T by suppressing spontaneous signal fluctuations. Neuroimage. Jan 15; 2009 44(2):448–454. [PubMed: 18835582]

133. Poser BA, Norris DG. Investigating the benefits of multi-echo EPI for fMRI at 7 T. Neuroimage. May 15; 2009 45(4):1162–1172. [PubMed: 19349231]

134. van der Zwaag W, Francis S, Head K, Peters A, Gowland P, Morris P, Bowtell R. fMRI at 1.5, 3 and 7 T: Characterising BOLD signal changes. Neuroimage. Oct 1; 2009 47(4):1425–1434. [PubMed: 19446641]

135. van der Zwaag W, Marques JP, Hergt M, Gruetter R. Investigation of high-resolution functional magnetic resonance imaging by means of surface and array radiofrequency coils at 7 T. Magn. Reson. Imag. Mar 3.2009 27:1011–1018.

136. Moeller S, Auerbach E, Van de Moortele P-F, Adriany G, Ugurbil K. fMRI with 16 fold reduction using multibanded multislice sampling. Proc. Int. Soc. Mag. Reson. Med. 2008; 16:2366.

137. Moeller S, Yacoub E, Olman CA, Auerbach E, Strupp J, Harel N, Ugurbil K. Multiband multislice GE-EPI at 7 tesla, with 16-fold acceleration using partial parallel imaging with application to high spatial and temporal whole-brain fMRI. Magn. Reson. Med. May; 2010 63(5):1144–1153. [PubMed: 20432285]

138. Breuer FA, Blaimer M, Heidemann RM, Mueller MF, Griswold MA, Jakob PM. Controlled aliasing in parallel imaging results in higher acceleration (CAIPIRINHA) for multi-slice imaging. Magn. Reson. Med. Mar; 2005 53(3):684–691. [PubMed: 15723404]

139. Breuer FA, Blaimer M, Mueller MF, Seiberlich N, Heidemann RM, Griswold MA, Jakob PM. Controlled aliasing in volumetric parallel imaging (2D CAIPIRINHA). Magn. Reson. Med. Mar; 2006 55(3):549–556. [PubMed: 16408271]

140. Setsompop K, Gagoski BA, Polimeni JR, Witzel T, Wedeen VJ, Wald LL. Blipped-controlled aliasing in parallel imaging for simultaneous multislice echo planar imaging with reduced g-factor penalty. Magn. Reson. Med. May; 2012 67(5):1210–1224. [PubMed: 21858868]

141. Xu J, Moeller S, Auerbach EJ, Strupp J, Smith SM, Feinberg DA, Yacoub E, Ugurbil K. Evaluation of slice accelerations using multiband echo planar imaging at 3 Tesla. Neuroimage. Jul 27.2013 83:991–1001. [PubMed: 23899722]

142. Norris DG, Koopmans PJ, Boyacioglu R, Barth M. Power Independent of number of Slices (PINS) radiofrequency pulses for low-power simultaneous multislice excitation. Magn. Reson. Med. Nov; 2011 66(5):1234–1240. [PubMed: 22009706]

143. Auerbach EJ, Xu J, Yacoub E, Moeller S, Ugurbil K. Multi-band accelerated spin-echo echo planar imaging with reduced peak RF power using time-shifted RF pulses. Magn. Reson. Med. May; 2013 69(5):1261–1267. [PubMed: 23468087]

144. Wu X, Vu AT, Schmitter S, Auerbach E, Moeller E, Lenglet C, Yacoub E, Van de Moortele P-F, Ugurbil K. Whole brain single shot diffusion weighted EPI at 7 Tesla using parallel transmit multislice multiband RF pulses. Proc. Int. Soc. Mag. Reson. Med. 2014; 22:311.

145. Wu X, Tian J, Schmitter S, Vaughan T, Ugurbil K, Van de Moortele P-F. Z-stacked RF array design enhances parallel transmit multi-band RF performance in whole brain simultaneous multislice imaging at 7 T. Proc. Int. Soc. Mag. Reson. Med. 2014; 22:543.

146. Wu X, Schmitter S, Ugurbil K, Van de Moortele P-F. Slab-wise parallel transmit multiband RF pulse design for simultaneous multislice imaging with volumetric coverage. Proc. Int. Soc. Mag. Reson. Med. 2014; 22:4333.

147. Barch DM, Burgess GC, Harms MP, Petersen SE, Schlaggar BL, Corbetta M, Glasser MF, Curtiss S, Dixit S, Feldt C, Nolan D, Bryant E, Hartley T, Footer O, Bjork JM, Poldrack R, Smith S, Johansen-Berg H, Snyder AZ, Van Essen DC, Consortium WU-MH. Function in the human connectome: Task-fMRI and individual differences in behavior. Neuroimage. Oct 15.2013 80:169–189. [PubMed: 23684877]

148. Sotiropoulos SN, Jbabdi S, Xu J, Andersson JL, Moeller S, Auerbach EJ, Glasser MF, Hernandez M, Sapiro G, Jenkinson M, Feinberg DA, Yacoub E, Lenglet C, Van Essen DC, Ugurbil K, Behrens TE, Consortium WU-MH. Advances in diffusion MRI acquisition and processing in the human connectome project. Neuroimage. Oct 15.2013 80:125–143. [PubMed: 23702418]

149. Van Essen DC, Smith SM, Barch DM, Behrens TE, Yacoub E, Ugurbil K, Consortium WU-MH. The WU-minn human connectome project: An overview. Neuroimage. Oct 15.2013 80:62–79. [PubMed: 23684880]

150. Smith SM, Beckmann CF, Andersson J, Auerbach EJ, Bijsterbosch J, Douaud G, Duff E, Feinberg DA, Griffanti L, Harms MP, Kelly M, Laumann T, Miller KL, Moeller S, Petersen S, Power J, Salimi-Khorshidi G, Snyder AZ, Vu AT, Woolrich MW, Xu J, Yacoub E, Ugurbil K, Van Essen DC, Glasser MF, Consortium WU-MH. Resting-state fMRI in the human connectome project. Neuroimage. Oct 15.2013 80:144–168. [PubMed: 23702415]

151. McNab JA, Edlow BL, Witzel T, Huang SY, Bhat H, Heberlein K, Feiweier T, Liu K, Keil B, Cohen-Adad J, Tisdall MD, Folkerth RD, Kinney HC, Wald LL. The human connectome project and beyond: Initial applications of 300 mT/m gradients. Neuroimage. Oct 15.2013 80:234–245. [PubMed: 23711537]

152. Setsompop K, Kimmlingen R, Eberlein E, Witzel T, Cohen-Adad J, McNab JA, Keil B, Tisdall MD, Hoecht P, Dietz P, Cauley SF, Tountcheva V, Matschl V, Lenz VH, Heberlein K, Potthast A, Thein H, Van Horn J, Toga A, Schmitt F, Lehne D, Rosen BR, Wedeen V, Wald LL. Pushing the limits of in vivo diffusion MRI for the human connectome project. Neuroimage. Oct 15.2013 80:220–233. [PubMed: 23707579]

153. Biswal B, Yetkin FZ, Haughton VM, Hyde JS. Functional connectivity in the motor cortex of resting human brain using echo-planar MRI. Magn. Reson. Med. Oct; 1995 34(4):537–541. [PubMed: 8524021]

154. Leopold DA, Murayama Y, Logothetis NK. Very slow activity fluctuations in monkey visual cortex: Implications for functional brain imaging. Cerebral Cortex. Apr; 2003 13(4):422–433. [PubMed: 12631571]

155. Nir Y, Hasson U, Levy I, Yeshurun Y, Malach R. Widespread functional connectivity and fMRI fluctuations in human visual cortex in the absence of visual stimulation. Neuroimage. May 1; 2006 30(4):1313–1324. [PubMed: 16413791]

156. De Martino F, Esposito F, Van de Moortele PF, Harel N, Formisano E, Goebel R, Ugurbil K, Yacoub E. Whole brain high-resolution functional imaging at ultra high magnetic fields: An application to the analysis of resting state networks. Neuroimage. Aug 1; 2011 57(3):1031–1044. [PubMed: 21600293]

157. Feinberg DA, Moeller S, Smith SM, Auerbach E, Ramanna S, Gunther M, Glasser MF, Miller KL, Ugurbil K, Yacoub E. Multiplexed echo planar imaging for sub-second whole brain FMRI and fast diffusion imaging. PLoS One. 2010; 5(12):e15710. [PubMed: 21187930]

158. Smith SM, Vidaurre D, Beckmann CF, Glasser MF, Jenkinson M, Miller KL, Nichols TE, Robinson EC, Salimi-Khorshidi G, Woolrich MW, Barch DM, Ugurbil K, Van Essen DC. Functional connectomics from resting-state fMRI. Trends Cogn. Sci. Dec; 2013 17(12):666–682. [PubMed: 24238796]

159. Norris DG. High field human imaging. J. Magn. Reson. Imag. Nov; 2003 18(5):519–529.

160. Henry TR, Chupin M, Lehericy S, Strupp JP, Sikora MA, Sha ZY, Ugurbil K, Van de Moortele PF. Hippocampal sclerosis in temporal lobe epilepsy: Findings at 7 T(1). Radiology. 2011 Oct; 261(1):199–209. [PubMed: 21746814]

161. Haacke EM, Xu Y, Cheng YC, Reichenbach JR. Susceptibility weighted imaging (SWI). Magn. Reson. Med. 2004 Sep; 52(3):612–618. [PubMed: 15334582]

162. Abosch A, Yacoub E, Ugurbil K, Harel N. An assessment of current brain targets for deep brain stimulation surgery with susceptibility-weighted imaging at 7 Tesla. Neurosurgery. Dec; 2010 67(6):1745–1756. [PubMed: 21107206]

163. Theysohn JM, Kraff O, Maderwald S, Barth M, Ladd SC, Forsting M, Ladd ME, Gizewski ER. 7 Tesla MRI of microbleeds and white matter lesions as seen in vascular dementia. J. Magn. Reson. Imag. Apr; 2011 33(4):782–791.

164. Lupo JM, Chuang CF, Chang SM, Barani IJ, Jimenez B, Hess CP, Nelson SJ. 7-Tesla susceptibility-weighted imaging to assess the effects of radiotherapy on normal-appearing brain in patients with glioma. Int. J. Radiat. Oncol. Biol. Phys. Mar 1; 2012 82(3):e493–e500. [PubMed: 22000750]
165. van Veluw SJ, Heringa SM, Kuijf HJ, Koek HL, Luijten PR, Biessels GJ. and Utrecht Vascular Cognitive Impairment Study. Cerebral cortical microinfarcts at 7 Tesla MRI in patients with early Alzheimer's disease. J. Alzheimers Dis. 2014; 39(1):163–167. [PubMed: 24121967]
166. Duyn JH. Study of brain anatomy with high-field MRI: Recent progress. Magn. Reson. Imag. Oct; 2010 28(8):1210–1215.
167. Duyn JH, van Gelderen P, Li TQ, de Zwart JA, Koretsky AP, Fukunaga M. High-field MRI of brain cortical substructure based on signal phase. Proc. Nat. Acad. Sci. USA. Jul 10; 2007 104(28):11796–11801. [PubMed: 17586684]
168. Shmueli K, Dodd SJ, Li TQ, Duyn JH. The contribution of chemical exchange to MRI frequency shifts in brain tissue. Magn. Reson. Med. Jan; 2011 65(1):35–43. [PubMed: 20928888]
169. Lee J, Hirano Y, Fukunaga M, Silva AC, Duyn JH. On the contribution of deoxy-hemoglobin to MRI gray-white matter phase contrast at high field. Neuroimage. Jan 1; 2010 49(1):193–198. [PubMed: 19619663]
170. Fukunaga M, Li TQ, van Gelderen P, de Zwart JA, Shmueli K, Yao B, Lee J, Maric D, Aronova MA, Zhang G, Leapman RD, Schenck JF, Merkle H, Duyn JH. Layer-specific variation of iron content in cerebral cortex as a source of MRI contrast. Proc. Nat. Academy Sci. USA. Feb 23; 2010 107(8):3834–3839.
171. Yao B, Li TQ, Gelderen P, Shmueli K, de Zwart JA, Duyn JH. Susceptibility contrast in high field MRI of human brain as a function of tissue iron content. Neuroimage. Feb 15; 2009 44(4): 1259–1266. [PubMed: 19027861]
172. Zhong K, Leupold J, von Elverfeldt D, Speck O. The molecular basis for gray and white matter contrast in phase imaging. Neuroimage. May 1; 2008 40(4):1561–1566. [PubMed: 18353683]
173. Marques JP, Maddage R, Mlynarik V, Gruetter R. On the origin of the MR image phase contrast: An in vivo MR microscopy study of the rat brain at 14.1 T. Neuroimage. Jun; 2009 46(2):345–352. [PubMed: 19254768]
174. Duyn J. MR susceptibility imaging. J. Magn. Reson. Apr.2013 229:198–207. [PubMed: 23273840]
175. Wharton S, Bowtell R. Whole-brain susceptibility mapping at high field: A comparison of multiple- and single-orientation methods. Neuroimage. Nov 1; 2010 53(2):515–525. [PubMed: 20615474]
176. Li X, Vikram DS, Lim IA, Jones CK, Farrell JA, van Zijl PC. Mapping magnetic susceptibility anisotropies of white matter in vivo in the human brain at 7 T. Neuroimage. Aug 1; 2012 62(1): 314–330. [PubMed: 22561358]
177. Bolan PJ, Yacoub E, Garwood M, Ugurbil K, Harel N. In vivo micro-MRI of intracortical neurovasculature. Neuroimage. Aug 1; 2006 32(1):62–69. [PubMed: 16675271]
178. Dobre MC, Marjanska M, Ugurbil K. Blood T_1 measurement at high magnetic field strength. Proc. Int. Soc. Mag. Reson. Med. 2005; 13:1162.
179. Cho ZH, Kang CK, Han JY, Kim SH, Park CA, Kim KN, Hong SM, Park CW, Kim YB. Functional MR angiography with 7.0 T is direct observation of arterial response during neural activity possible? Neuroimage. Aug 1; 2008 42(1):70–75. [PubMed: 18539047]
180. Cho ZH, Kang CK, Han JY, Kim SH, Kim KN, Hong SM, Park CW, Kim YB. Observation of the lenticulostriate arteries in the human brain in vivo using 7.0 T MR angiography. Stroke. May; 2008 39(5):1604–1606. [PubMed: 18340096]
181. Schmitter S, Wu X, Auerbach EJ, Adriany G, Pfeuffer J, Hamm M, Ugurbil K, Van de Moortele PF. Seven-tesla time-of-flight angiography using a 16-channel parallel transmit system with power-constrained 3-dimensional spoke radiofrequency pulse design. Invest Radiol. May; 2014 49(5):314–325. [PubMed: 24598439]
182. van de Bank BL, Voogt IJ, Italiaander M, Stehouwer BL, Boer VO, Luijten PR, Klomp DW. Ultra high spatial and temporal resolution breast imaging at 7 T. NMR Biomed. 2013; 26(4):367–375.

183. Brunner DO, De Zanche N, Frohlich J, Paska J, Pruessmann KP. Travelling-wave nuclear magnetic resonance. Nature. Feb 19; 2009 457(7232):994–998. [PubMed: 19225521]

184. Metzger GJ, Auerbach EJ, Akgun C, Simonson J, Bi X, Ugurbil K, Van de Moortele PF. Dynamically applied B1+ shimming solutions for non-contrast enhanced renal angiography at 7.0 Tesla. Magn. Reson. Med. Jan; 2013 69(1):114–126. [PubMed: 22442056]

185. Snyder CJ, Delabarre L, Moeller S, Tian J, Akgun C, Van de Moortele PF, Bolan PJ, Ugurbil K, Vaughan JT, Metzger GJ. Comparison between eight- and sixteen-channel TEM transceive arrays for body imaging at 7 T. Magn. Reson. Med. Apr; 2012 67(4):954–964. [PubMed: 22102483]

186. Ellermann J, Goerke U, Morgan P, Ugurbil K, Tian J, Schmitter S, Vaughan T, Van de Moortele PF. Simultaneous bilateral hip joint imaging at 7 Tesla using fast transmit B(1) shimming methods and multichannel transmission—A feasibility study. NMR Biomed. Oct; 2012 25(10): 1202–1208. [PubMed: 22311346]

187. Grams AE, Kraff O, Umutlu L, Maderwald S, Dammann P, Ladd ME, Forsting M, Gizewski ER. MRI of the lumbar spine at 7 Tesla in healthy volunteers and a patient with congenital malformations. Skeletal Radiol. May 24.2011 41:509–514. [PubMed: 21604210]

188. Orzada S, Maderwald S, Poser BA, Bitz AK, Quick HH, Ladd ME. RF excitation using time interleaved acquisition of modes (TIAMO) to address B1 inhomogeneity in high-field MRI. Magn. Re-son. Med. Aug; 2010 64(2):327–233.

189. Umutlu L, Kraff O, Orzada S, Fischer A, Kinner S, Maderwald S, Antoch G, Quick HH, Forsting M, Ladd ME, Lauenstein TC. Dynamic contrast-enhanced renal MRI at 7 Tesla: Preliminary results. Investigative Radiol. Jul; 2011 46(7):425–433.

190. Umutlu L, Orzada S, Kinner S, Maderwald S, Brote I, Bitz AK, Kraff O, Ladd SC, Antoch G, Ladd ME, Quick HH, Lauenstein TC. Renal imaging at 7 Tesla: Preliminary results. Eur. Radiol. Apr; 2011 21(4):841–849. [PubMed: 20872006]

191. Frauenrath T, Hezel F, Heinrichs U, Kozerke S, Utting JF, Kob M, Butenweg C, Boesiger P, Niendorf T. Feasibility of cardiac gating free of interference with electro-magnetic fields at 1.5 Tesla, 3.0 Tesla and 7.0 Tesla using an MR-stethoscope. Investigative Radiol. Sep; 2009 44(9): 539–547.

192. Frauenrath T, Hezel F, Renz W, d'Orth Tde G, Dieringer M, von Knobelsdorff-Brenkenhoff F, Prothmann M, Schulz Menger J, Niendorf T. Acoustic cardiac triggering: A practical solution for synchronization and gating of cardiovascular magnetic resonance at 7 Tesla. J. Cardiovasc. Magn. Reson. 2010; 12, p(67)

193. von Knobelsdorff-Brenkenhoff F, Frauenrath T, Prothmann M, Dieringer MA, Hezel F, Renz W, Kretschel K, Niendorf T, Schulz-Menger J. Cardiac chamber quantification using magnetic resonance imaging at 7 Tesla—A pilot study. Eur. Radiol. Dec; 2010 20(12):2844–5282. [PubMed: 20640427]

194. van Elderen SG, Versluis MJ, Webb AG, Westenberg JJ, Doornbos J, Smith NB, de Roos A, Stuber M. Initial results on in vivo human coronary MR angiography at 7 T. Magn. Reson. Med. Dec; 2009 62(6):1379–1384. [PubMed: 19859918]

195. von Knobelsdorff-Brenkenhoff F, Tkachenko V, Winter L, Rieger J, Thalhammer C, Hezel F, Graessl A, Dieringer MA, Niendorf T, Schulz-Menger J. Assessment of the right ventricle with cardiovascular magnetic resonance at 7 Tesla. J. Cardiovasc Magn. Reson. 2013; 15(23):1–9. [PubMed: 23324167]

196. Graessl A, Renz W, Hezel F, Dieringer MA, Winter L, Oezerdem C, Rieger J, Kellman P, Santoro D, Lindel TD, Frauenrath T, Pfeiffer H, Niendorf T. Modular 32-channel transceiver coil array for cardiac MRI at 7.0 T. Magn. Reson. Med. 2013

197. Maas MC, Vos EK, Lagemaat MW, Bitz AK, Orzada S, Kobus T, Kraff O, Maderwald S, Ladd ME, Scheenen TW. Feasibility of T-weighted turbo spin echo imaging of the human prostate at 7 Tesla. Magn. Reson. Med. Jun 24.2013

198. Raaijmakers AJ, Ipek O, Klomp DW, Possanzini C, Harvey PR, Lagendijk JJ, van den Berg CA. Design of a radiative surface coil array element at 7 T: The single-side adapted dipole antenna. Magn. Reson. Med. Nov; 2011 66(5):1488–1497. [PubMed: 21630342]

199. Schmitter S, Ugurbil K, Van de Moortele P-F. Multi-band-multi-spoke pTX RF pulse design in the heart at 7 Tesla: Towards faster, uniform contrast cardiac CINE imaging. Proc. Int. Soc. Mag. Reson. Med. 2014; 22:626.

200. de Greef M, Ipek O, Raaijmakers AJ, Crezee J, van den Berg CA. Specific absorption rate intersubject variability in 7 T parallel transmit MRI of the head. Magn. Reson. Med. May; 2013 69(5):1476–1485. [PubMed: 22760930]

201. Jin J, Liu F, Weber E, Crozier S. Improving SAR estimations in MRI using subject-specific models. Phys. Med. Biol. Dec 21; 2012 57(24):8153–8171. [PubMed: 23174940]

202. Ipek O, Raaijmakers AJ, Lagendijk JJ, Luijten PR, van den Berg CA. Intersubject local SAR variation for 7 T prostate MR imaging with an eight-channel single-side adapted dipole antenna array. Magn. Reson. Med. Jun 10.2013

203. Van den Berg CA, van den Bergen B, Van de Kamer JB, Raaymakers BW, Kroeze H, W Bartels L, Lagendijk JJ. Simultaneous B1+ homogenization and specific absorption rate hotspot suppression using a magnetic resonance phased array transmit coil. Magn. Reson. Med. Mar; 2007 57(3):577–586. [PubMed: 17326185]

204. Setsompop K, Wald LL, Alagappan V, Gagoski B, Hebrank F, Fontius U, Schmitt F, Adalsteinsson E. Parallel RF transmission with eight channels at 3 Tesla. Magn. Reson. Med. Nov; 2006 56(5):1163–1171. [PubMed: 17036289]

205. Homann H, Graesslin I, Eggers H, Nehrke K, Vernickel P, Katscher U, Dossel O, Bornert P. Local SAR management by RF shimming: A simulation study with multiple human body models. MAGMA. Jun; 2012 25(3):193–204. [PubMed: 21922191]

206. Brunner DO, Pruessmann KP. Optimal design of multiple-channel RF pulses under strict power and SAR constraints. Magn. Reson. Med. May; 2010 63(5):1280–1291. [PubMed: 20432299]

207. Lee J, Gebhardt M, Wald LL, Adalsteinsson E. Local SAR in parallel transmission pulse design. Magn. Reson. Med. Jun; 2012 67(6):1566–1578. [PubMed: 22083594]

208. Guerin B, Gebhardt M, Cauley S, Adalsteinsson E, Wald LL. Local specific absorption rate (SAR), global SAR, transmitter power, and excitation accuracy trade-offs in low flip-angle parallel transmit pulse design. Magn. Reson. Med. Jun 14.2013 71:1446–1457. [PubMed: 23776100]

209. Guerin B, Adalsteinsson E, Wald LL. Local SAR reduction in multi-slice pTx via “SAR hopping” between excitations. Proc. Int. Soc. Mag. Reson. Med. 2012; 20:642.

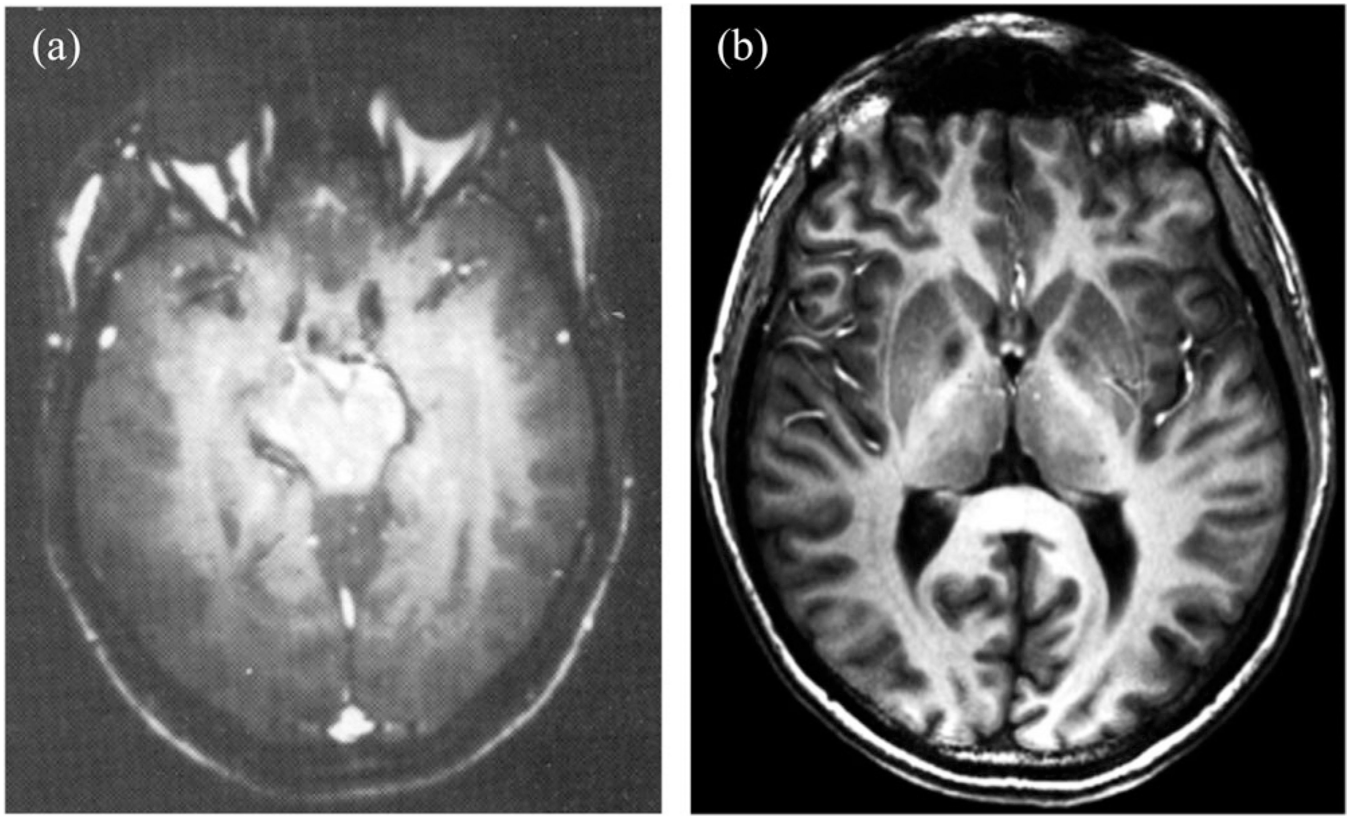

Fig. 1.
(a): Early 4 T brain images published from Siemens [10], [11]. (b) 4 T MDEFT images of human brain obtained in CMRR [12], [13].

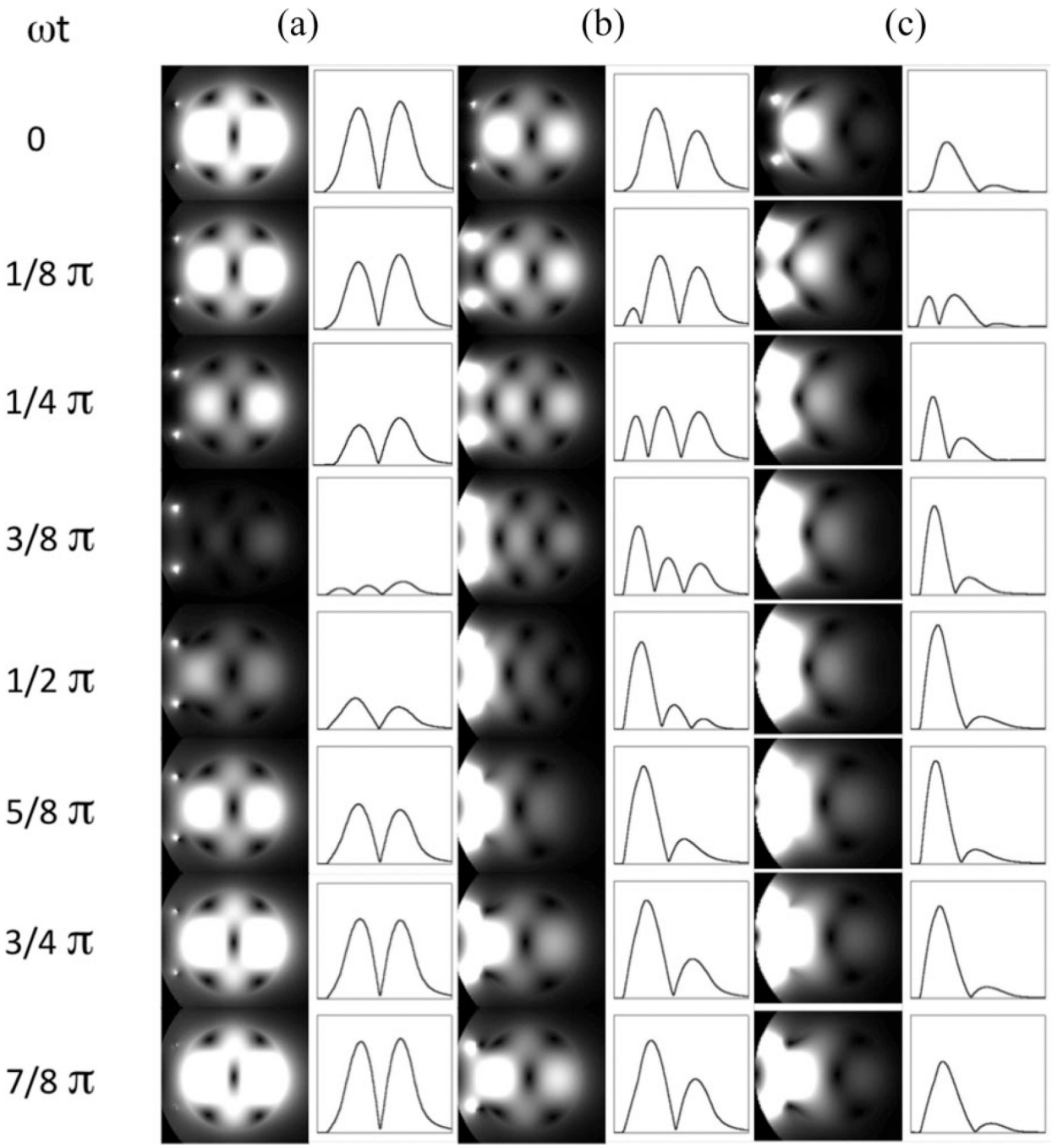

Fig. 2.

2-D plots of instantaneous transverse $|B_1|$ at progressing points during a half period in phantoms with (a) $\sigma = 0$ S/m, (b) $\sigma = 0.26$ S/m, and (c) $\sigma = 0.67$ S/m. The intensity profiles along the horizontal centerlines are also shown on the right of the 2-D plots. The surface coil position is indicated by two small dots on the left side of the phantom. Since the temporal B_1 strength varies greatly among these three cases, the signal intensities of temporal points are normalized individually for each conductivity condition in order to visualize the temporal change for all the conditions clearly [32].

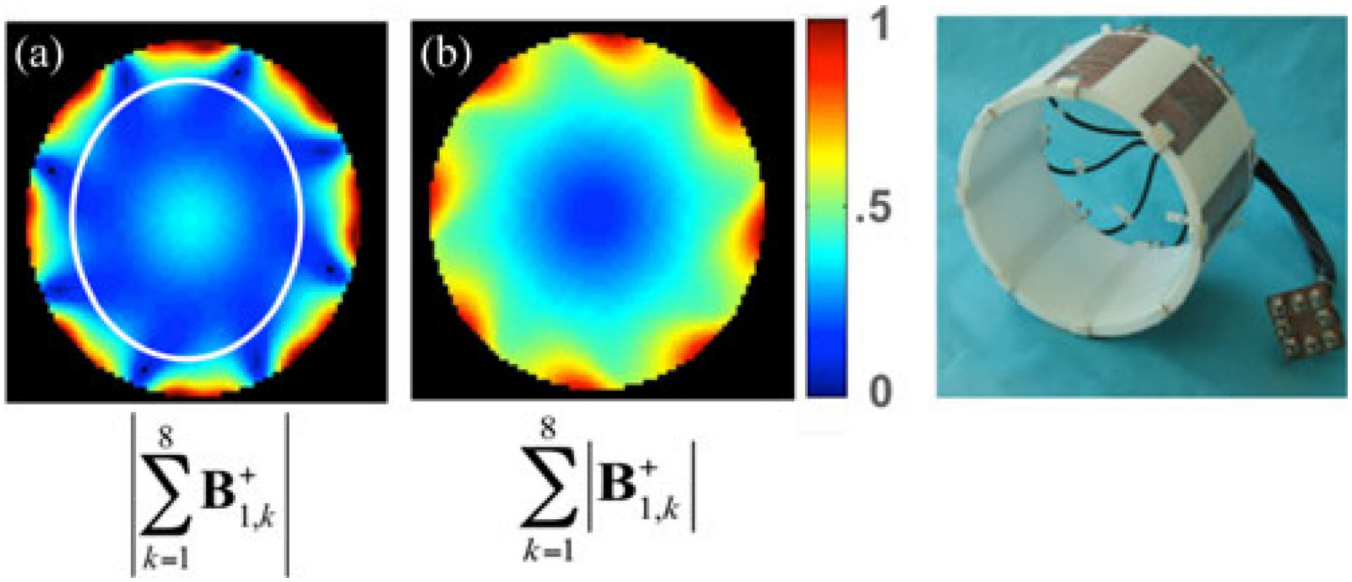

Fig. 3.

Transmit B_1 magnitude (color coded normalized intensity; see online version for color map) in a cylindrical "phantom" when the individual transmit B_1 vectors from each channel are first experimentally determined and subsequently are added according to the constructs shown below each figure from an eight channel transmit and receive RF coil where experiments were performed transmitting one channel at a time and receiving with all channels [33]. The white ellipse in A depicts approximate boundaries of a human head.

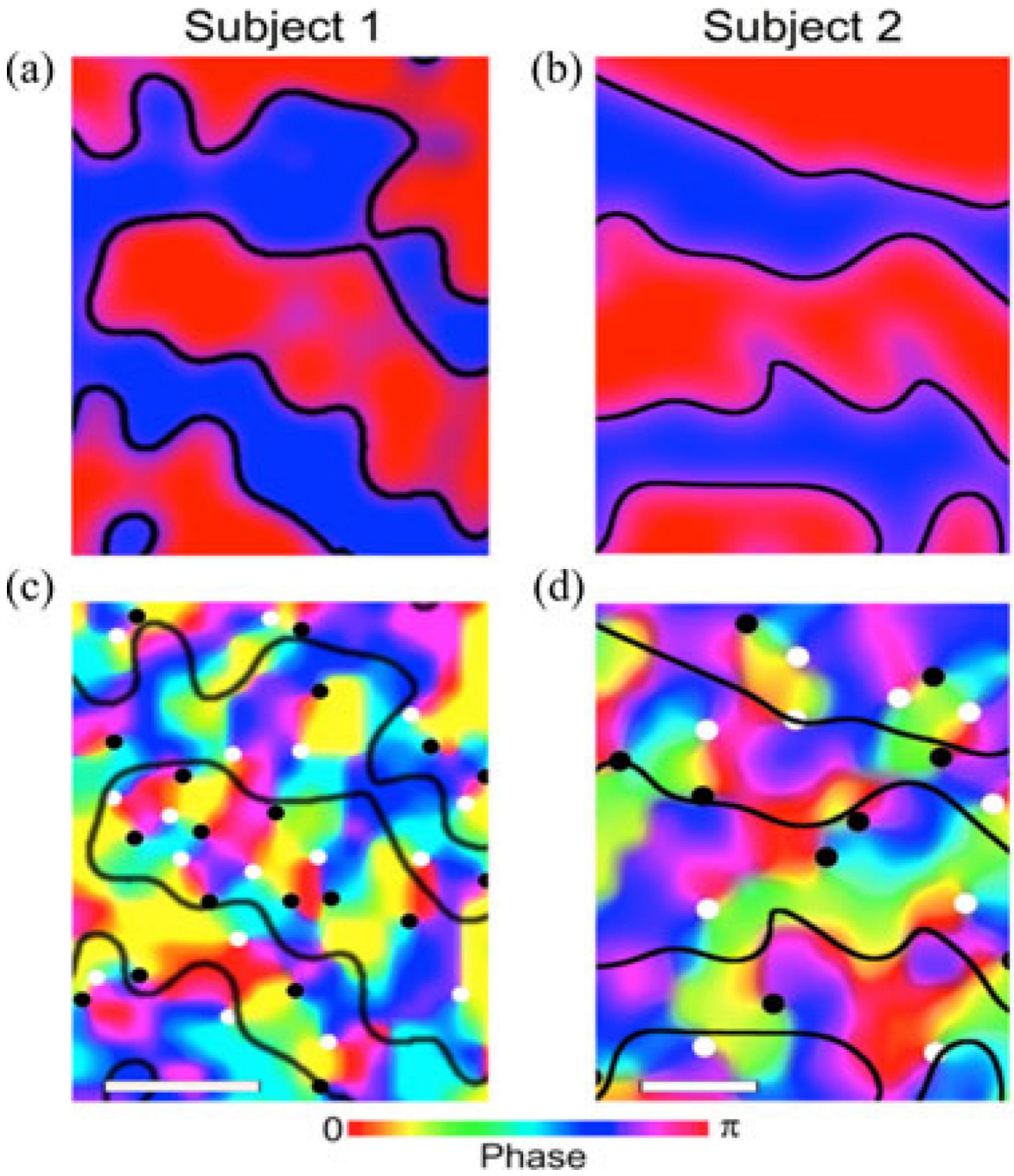

Fig. 4.

Functional maps of ocular dominance columns (a, b) and orientation columns (c, d) in the human brain obtained with SE fMRI at 7 T in two subjects (color coded; see online version for color Map). The black lines in (c), and (d) depict the boundaries of the ocular dominance columns seen in (a) and (b), respectively, so as to permit the visualization of the relationship between the two columnar organizations. The black and white dots in (c) and (d) identify the centers of clockwise and counterclockwise rotating pinwheels. The white bars (lower left hand corner in (c) and (d) designate 1 mm scale. From Yacoub *et al*. 2008 [74].

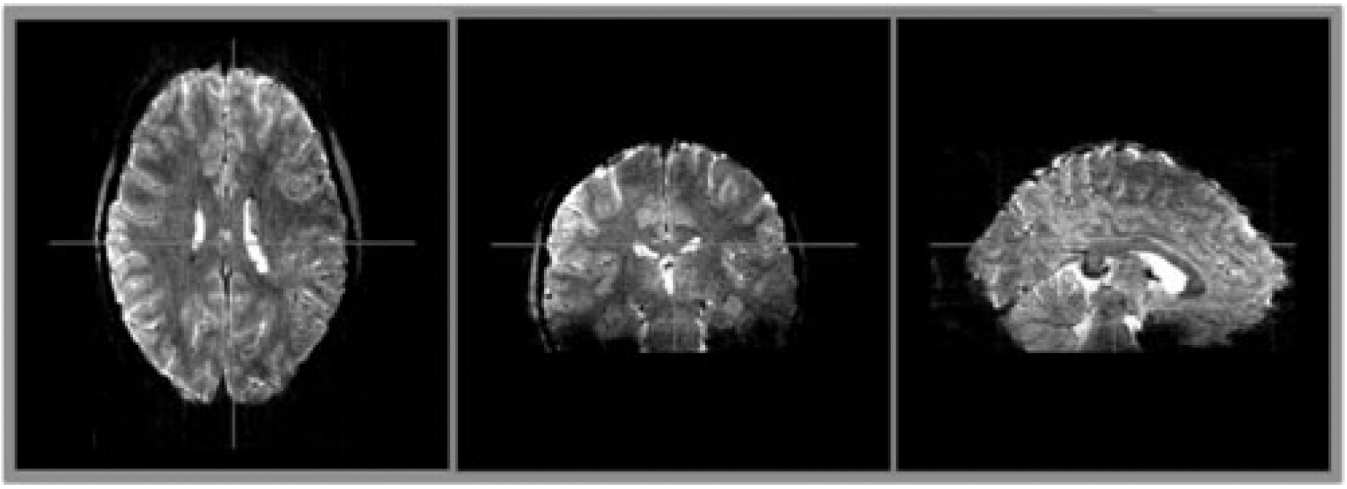

Fig. 5.

Multiband GRE EPI data acquired at 7 T with concurrent slice and in-plane (phase encode) acceleration (4 and 3 fold, respectively). Three orthogonal slices are shown from a 1-mm isotropic resolution whole brain data obtained with a 32 channel receive array and blipped CAIPI [140] field of view shift equivalent to FOV/3 (images provided by CMRR [118]).

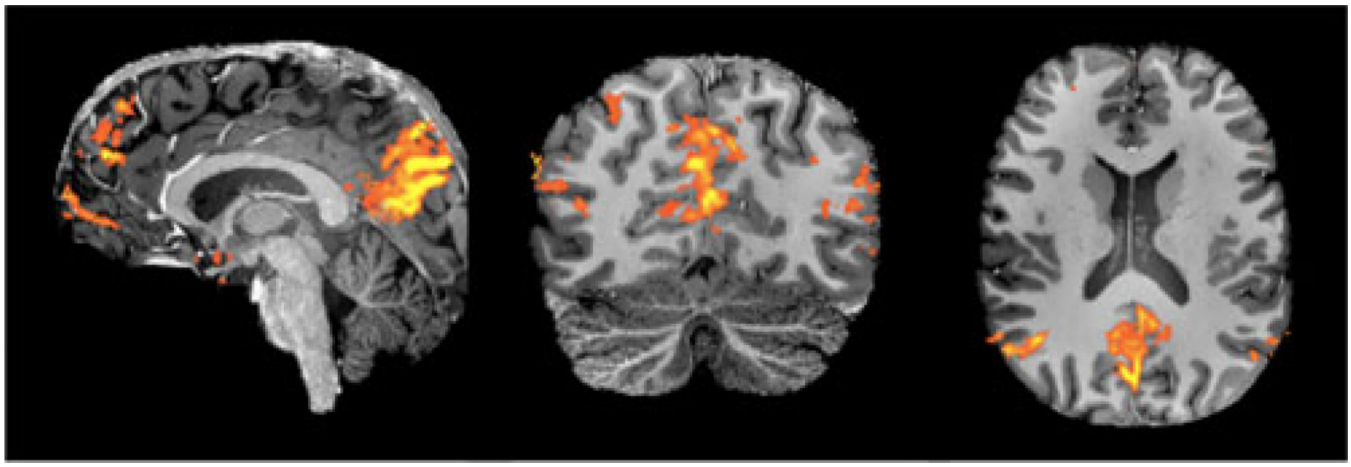

Fig. 6.

A resting state network [the so-called default mode network (DMN)] (shown in color superimposed on anatomical images in gray scale). extracted using independent component analysis (ICA) from 1-mm isotropic resolution, whole-brain 7 T rfMRI time series. Three orthogonal planes from the whole brain data are shown. Data were acquired using standard GRE EPI without slice acceleration but with 4-fold acceleration along the in-plane phase encode direction. The DMN data in color is superimposed on 0.6-mm isotropic T_1 weighted anatomical images obtained with MPRAGE at 7 T. Adapted from [156].

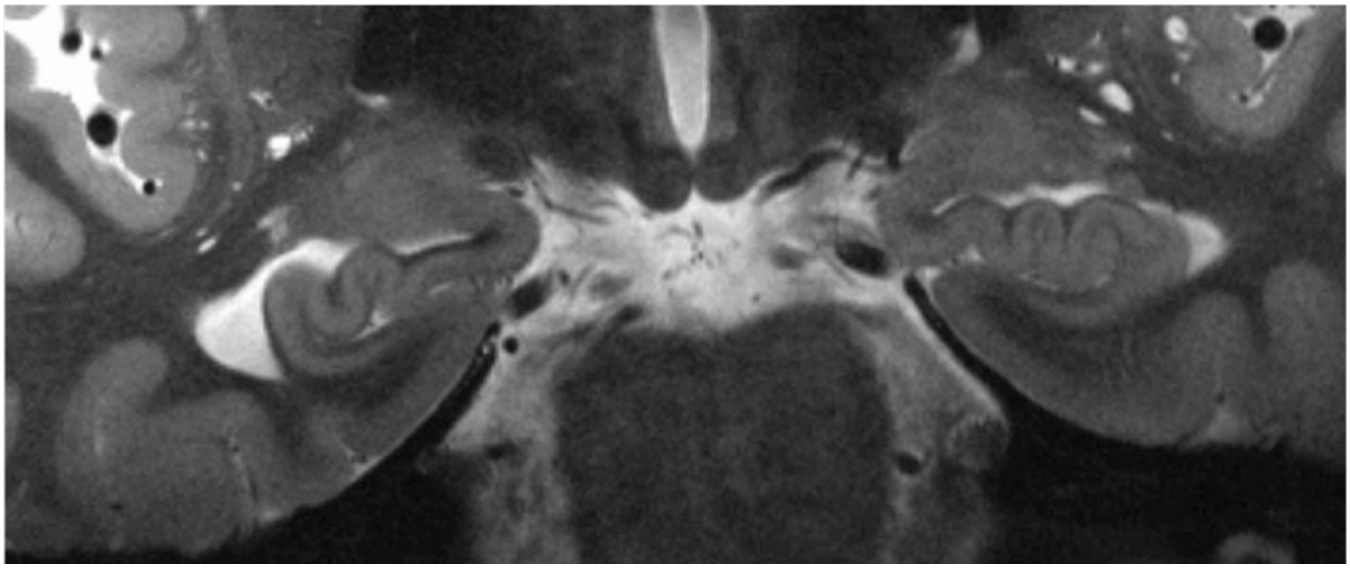

Fig. 7.

T_2-weighted MR images of the head of hippocampus obtained at 7 T in a coronal slice, from a control subject (31-year-old male). Adapted from [160].

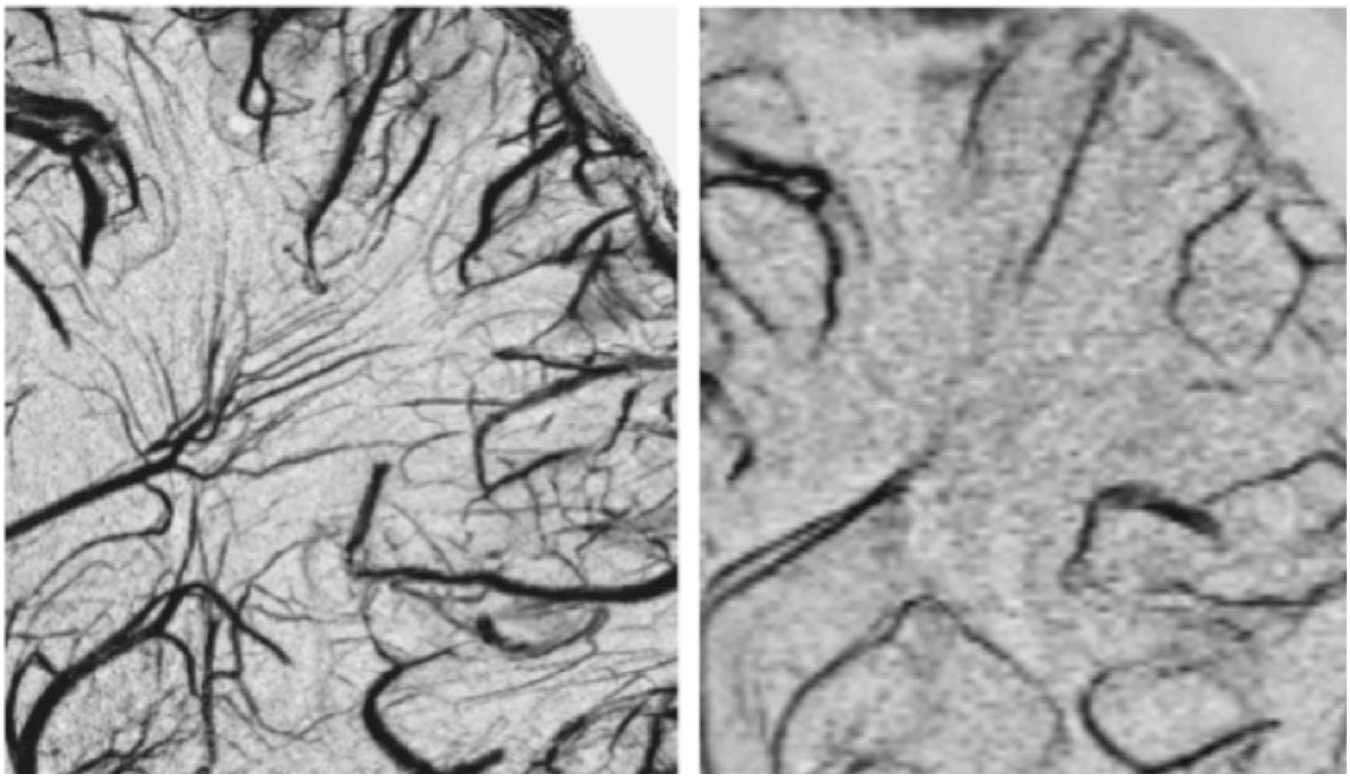

Fig. 8.
Susceptibility weighted imaging (SWI) at 9.4 T (left) and 3 T (right) in the human brain to depict venous anatomy (adapted from [103]).

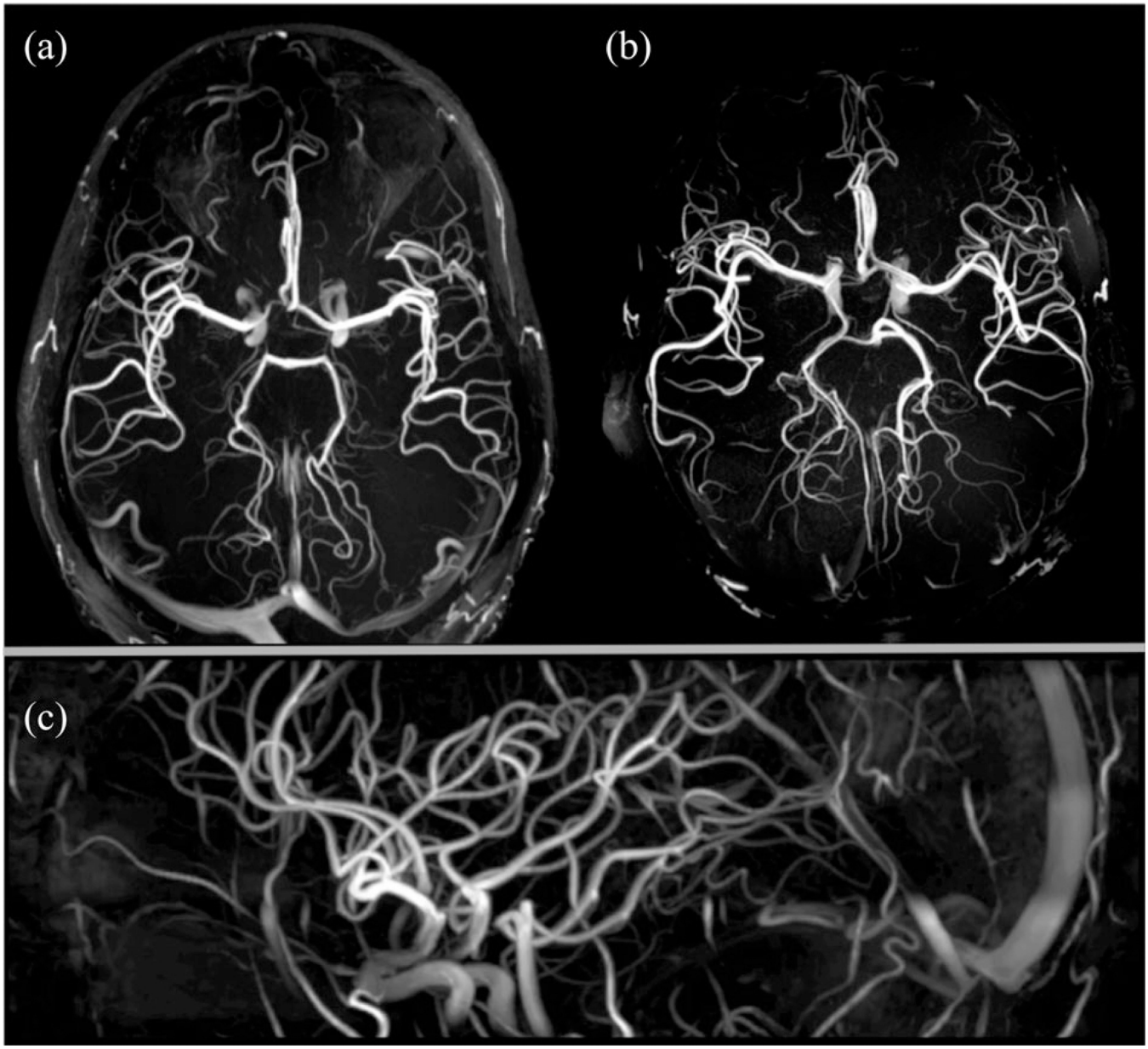

Fig. 9.

Time-of-flight angiography at 7 T viewed as a maximum intensity, projection in the axial (two different subjects and methods, a and b) and sagittal (c) orientations. Data were obtained using multichannel transmit to improve spatial homogeneity of the RF pulses employed in the acquisition (a and c) versus the standard circularly polarized mode acquisition. Adapted from [55] and [181].

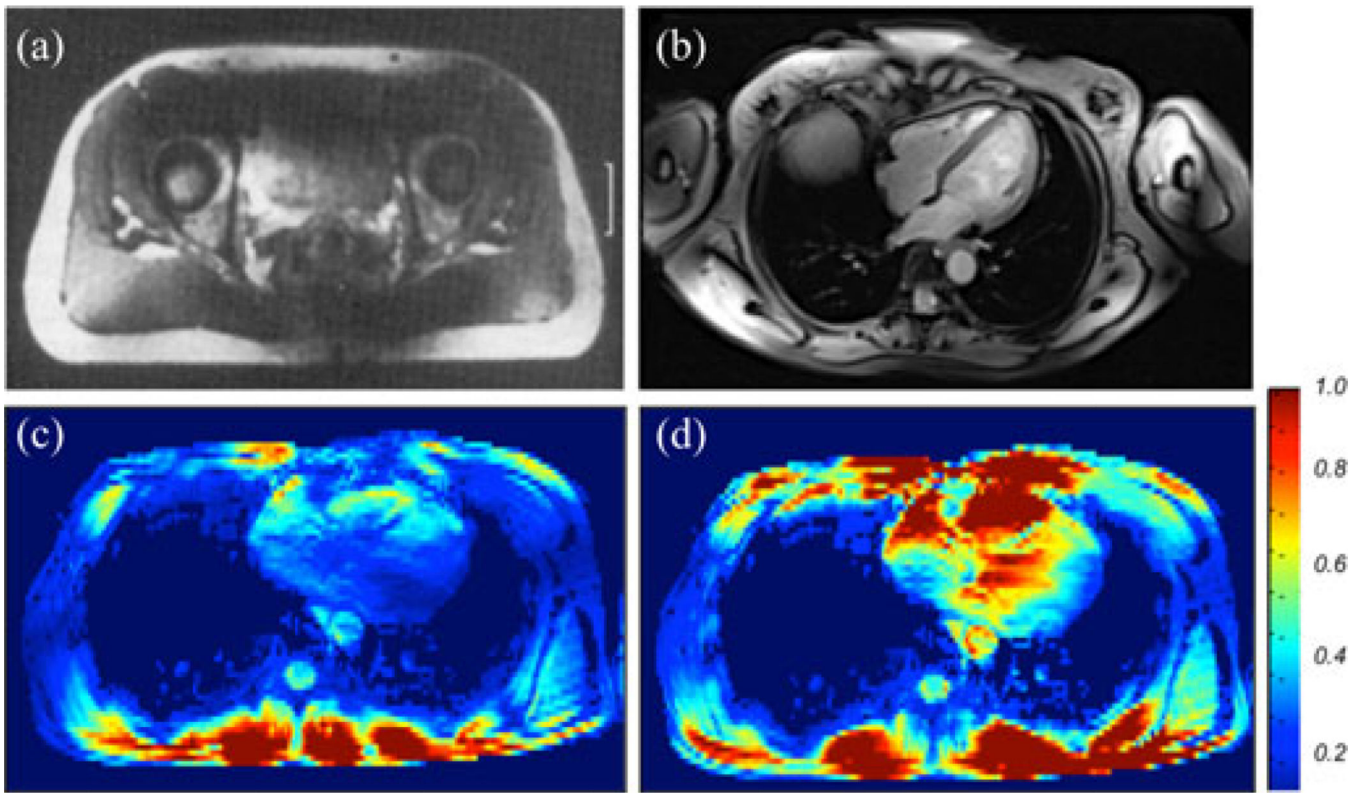

Fig. 10.

(a) Single slice body image reported from early 4 T experiments from the research laboratories of Siemens [1], [2]. (b) A contemporary 7 T image of a slice in the human torso, targeting imaging of the heart, obtained with a 16-channel transmit and receive array coil [48], [49], using B_1 "shimming" (image provided by C. J. Synder, L. DeLaBarre, and T. Vaughan) (c) and (d) The transmit B_1 magnitude map (normalized intensity, color coded) before (c) and after (d) optimization over the heart, demonstrating that the B_1 is normally highly inhomogeneous and weak over this organ of interest (c), but can be improved significantly by multichannel transmit methods (d) [48], [49].

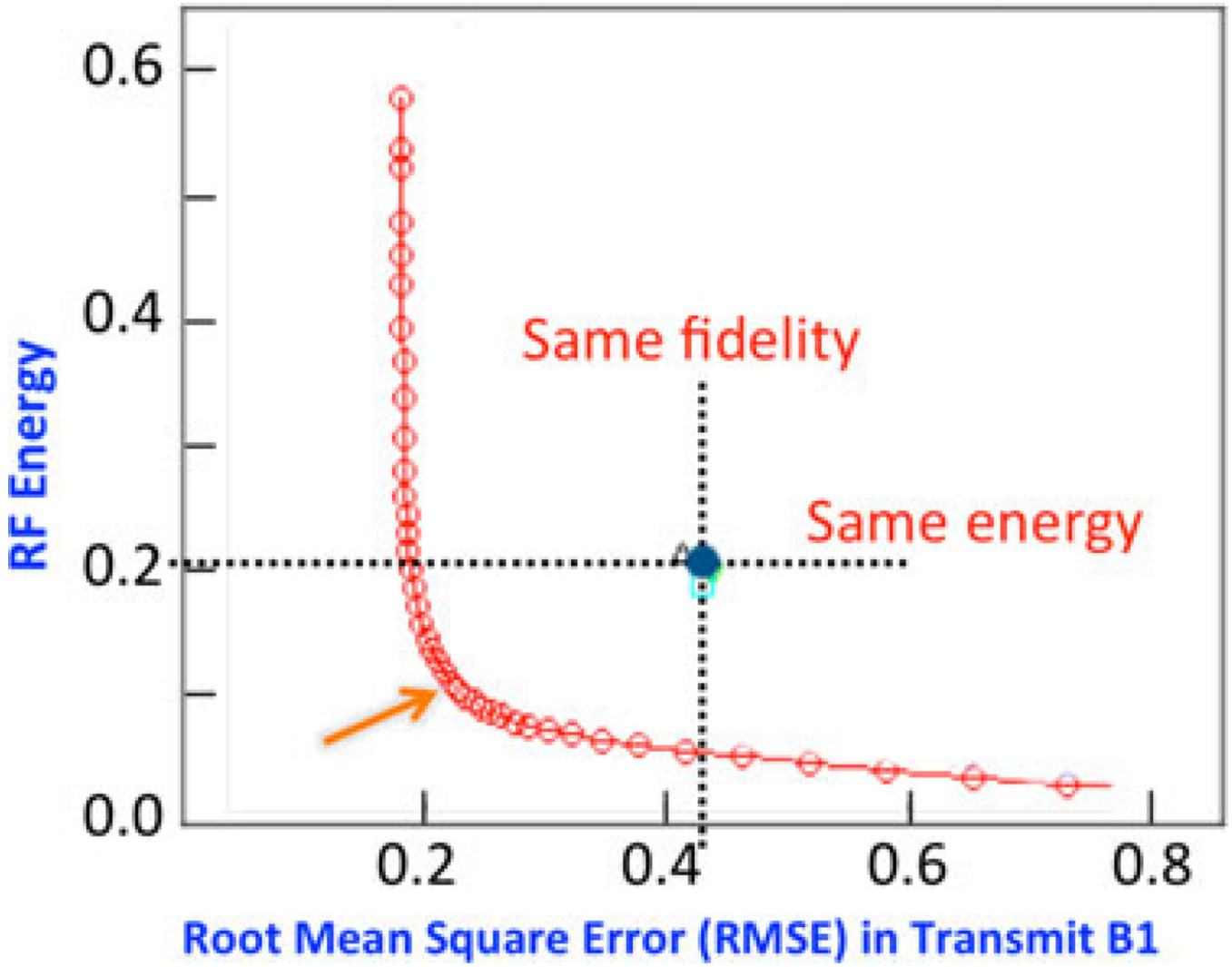

Fig. 11.

Sixteen channel pTx pulse design for a multiband RF pulse that excites two slices simultaneously in the human brain at 7 T. The L shaped curve quantifies tradeoffs, in this specific case, between total RF energy of the RF pulse and excitation errors [i.e., root mean square error (RMSE)]. The crossing between the horizontal and vertical dashed lines, labeled “Same fidelity” and “Same energy,” identify the performance of the same coil operated in a circularly polarized mode. Adapted from [64].